2018-05

The ultimate fate of a synmagmatic shear zone. Interplay between rupturing and ductile flow in a cooling granite pluton

Zibra, I

10.1016/j.jsg.2018.02.001
Journal of Structural Geology
Elsevier

The ultimate fate of a synmagmatic shear zone. Interplay between rupturing and ductile flow in a cooling granite pluton.

I Zibra, JC White, L Menegon, G Dering and K Gessner

Corresponding author: Ivan Zibra (ivan.zibra@dmirs.wa.gov.au)

Geological Survey of Western Australia

Department of Mines and Petroleum

100 Plain Street East Perth WA 6004

Tel: +61 8 9222 3082

Keywords:

Rupture; cataclasite; mylonite; tourmaline; transpression; strain partitioning

Abstract

The Neoarchean Cundimurra Pluton (Yilgarn Craton, Western Australia) was emplaced incrementally along the transpressional Cundimurra Shear Zone. During syndeformational cooling, discrete networks of cataclasites and ultramylonites developed in the narrowest segment of the shear zone, showing the same kinematics as the earlier synmagmatic structures. Lithological boundaries between aplite/pegmatite veins and host granitic gneiss show more intense pre-cataclasite fabrics than homogeneous material, and these boundaries later became the preferred sites of shear rupture and cataclasite nucleation.

Transient ductile instabilities established along lithological boundaries culminated in shear rupture at relatively high temperature (~500–600°C). Here, tensile fractures at high angles from the fault plane formed asymmetrically on one side of the fault, indicating development during seismic rupture, establishing the oldest documented earthquake on Earth.

Tourmaline veins were emplaced during brittle shearing, but fluid pressure probably played a minor role in brittle failure, as cataclasites are in places tourmaline-free. Subsequent ductile deformation localized in the rheologically weak tourmaline-rich aggregates, forming ultramylonites that deformed by grain-size sensitive creep. The shape and width of the pluton/shear zone and the regime of strain partitioning, induced by melt-present deformation and established during pluton emplacement, played a key role in controlling the local distribution of brittle and then ductile subsolidus structures.

1 Introduction

The mid- to upper continental crust, particularly during the early history of Earth, is dominated by intermediate-to-felsic intrusive rocks (Christensen and Mooney, 1995), thus the deformation behaviour of such bodies is critical to understanding of tectonic processes within continental lithosphere. Subsolidus strain localization in granitic rocks can be summarised in terms of two different models. In one model, strain hardening (Hobbs et al., 1990) or strain— and thermal—softening (White et al., 1980; Mancktelow, 2002; Thielmann and Kaus, 2012; Jaquet and

Schmalholz, 2017) controls the nucleation of shear zones. Deformation is thereby localised in an otherwise grossly isotropic medium lacking pervasive anisotropies such as flow layering, foliations or fractures. In the second model, inherited and precursor structures play a key role for localizing the development of ductile shear zones (Christiansen and Pollard, 1997; Guermani and Pennacchioni, 1998; Mancktelow and Pennacchioni, 2005; Pennacchioni and Mancktelow, 2007; Menegon and Pennacchioni, 2010; Goncalves et al., 2016). In the past decade, detailed field studies have demonstrated that anisotropies, such as cooling joints and lithological boundaries, play a key role in controlling the development of subsolidus shear zones in the mid-crust (Pennacchioni and Zucchi, 2013, and references therein). However, most of these studies focussed on the development of subsolidus outcrop- to grain-scale structures, so that the role of larger (i.e. km-scale) structures developed during pluton emplacement, and the role of a pluton itself in influencing the local strain distribution, is less well understood (Blanquat et al., 2011). If fault initiation and propagation styles are scale-variant (Crider, 2015), determining causes for strain localization at the regional scale, remains central to achieving understanding about deformation in the intermediate to felsic igneous rocks of the continental crust.

This contribution documents subsolidus deformation in the Neoarchean Cundimurra Pluton, from the Yilgarn Craton of Western Australia. This pluton was emplaced incrementally over a period of c. 20 Myr, along an active, triclinic transpressional shear zone (the Cundimurra Shear Zone, CMSZ; (Zibra et al., 2014b). The structures related to subsolidus overprinting exhibit the same kinematics as the synmagmatic CMSZ and provide an exceptional opportunity to examine the transiently discontinuous response within a ductile shear zone undergoing syndeformational cooling. We show that the post-magmatic stages of shear zone activity were characterized by the development of discrete fault networks comprising cataclasites and ultramylonites. Both ductile and brittle subsolidus structures are postdated by a c. 2620 Ma pluton, and are therefore of Neoarchean age. We document brittle structures within regional-scale fault networks containing evidence of a rupture episode at seismic velocities, with subsequent aseismic displacement along cataclasites and ultramylonites. Consequently, to the best of our knowledge, brittle faults within the CMSZ

preserve paleoseismic record of the oldest earthquakes yet documented on Earth. Our data reveal that brittle behaviour was transient, with a return to ductile deformation in the last stage. We propose that the regional-scale architecture of the shear zone and the melt-induced strain partitioning of the bulk triclinic flow, both of which were established during pluton emplacement, played a major role in controlling the subsolidus evolution of the cooling pluton.

2 Geological setting

The Archean Yilgarn Craton of Western Australia consists of c. 3050–2600 Ma granites and granitic gneisses associated with c. 3080–2650 Ma greenstone belts (i.e. metamorphosed volcano-sedimentary sequences and gabbroic sills). Lu–Hf and Sm—Nd isotopic data indicate that the craton recorded older crust-forming events, dating back to c. 4200 Ma (Wyche et al., 2012). The craton has been subdivided into several terranes on the basis of stratigraphic, structural, geochemical and geochronological data (Cassidy et al., 2006; Fig. 1a). In the c. 2730–2620 Ma time span, a major episode of magmatism and crustal recycling occurred during the Neoarchean Yilgarn Orogeny (Zibra et al., 2017a), and resulted in the assembly of several terranes to form the Yilgarn Craton (Myers, 1995). Seismic profiles show that boundaries between different terrains are represented by crustal-scale, east-dipping listric shear zones (Wilde et al., 1996; Goleby et al., 2004; Wyche et al., 2013) that are sub-parallel to the internal structural grain of each individual terrane.

In the western portion of the craton (Youanmi Terrane, Fig.1a), such networks of east-dipping crustal-scale shear zones accompanied the emplacement of large batholiths, controlling the delivery of Tonalite–Trondhjemite–Granodiorite (TTG) melt from its lower crustal source towards sink regions in the upper crust (Zibra et al., 2014a, 2017a, 2017b). In the centre of the Youanmi Terrane, the dextral transpressional Cundimurra Shear Zone (CMSZ, Fig. 1b) was active for >20 Myr, during the incremental emplacement of the Cundimurra Pluton (Zibra et al., 2014b). Displacement along the CMSZ continued after pluton assembly, during the syndeformational cooling of the granite-greenstone system.

The main gneissic foliation in the CMSZ developed under lower amphibolite facies conditions in both granites ($S_{MT;}$ moderate temperature foliation) and greenstones (S_G; figs 5–7 in Zibra et al., 2014b). Higher temperature (magmatic to solid-state) fabrics are locally preserved, mainly in the central segment of the CMSZ. The regional strain was strongly partitioned along the CMSZ, such that greenstone-derived tectonites accommodated the bulk of horizontal shortening and dip-parallel components of regional displacement, while granitic gneiss accommodated the strike-parallel component (Fig. 1c). The strike-parallel-dominated portion of the shear zone is ~17 km wide in the central and southern portions of the pluton, narrowing to ~2.5 km in the northeast-trending, northernmost part of the pluton (Fig.1b). The CMSZ extends for ~160 km north of the study area, towards the northern margin of the craton (Fig.1a), where it is truncated by Proterozoic structures. In its northern segment, outside of the study area, the CMSZ is entirely developed within greenstone sequences, where it splits into several synthetic branches, exploiting infra-greenstone lithological boundaries. The CMSZ, as with all the structures in the area, is post-dated by the c. 2620 Ma Garden Rock Monzogranite ("GR", Fig.1b; Zibra et al., 2014b), which shows concentric (i.e. pluton-parallel) magmatic foliation (inset d, Fig. 2), discordant to the CMSZ.

3 The Lake Austin Shear Zone: geometry and kinematics

The Lake Austin Shear Zone (LASZ) is a composite strike-slip structure exposed within the northern portion of the Cundimurra Pluton (Figs. 1 and 2). This structure postdates S_{MT}, extends ~33 km along strike and is developed entirely within the granitic gneiss. The LASZ postdates the c. 2660 Ma youngest leucogranite component of the pluton (Zibra et al., 2014b) and shows no evidence of melt-present deformation, being developed solely under subsolidus conditions.

Based on distinctive meso- and microstructures, the LASZ can be subdivided into three domains, which are, from north to south, the Pinnacles fault, the Golconda mylonite and the Moyagee fault (Fig. 2). The Moyagee and Pinnacles faults are characterized by networks of discrete cataclasite and ultramylonite zones, and are linked and postdated by the ~ 3 km-wide Golconda mylonite, which include

granitic gneiss whose fabric exhibits geometry and kinematics identical to S_{MT} (Fig. 2).

3.1 The Moyagee fault

The Moyagee fault (Figs. 2 and 3) contains a network of cataclasites and ultramylonites postdating S_{MT}. The network is sub-parallel to the western pluton boundary. It is exposed for ~7.5 km along strike, with a maximum width of ~1.5 km, near its central portion. Scaling and topology of the fault array were documented by integrating field observations with millimetre-resolution digital orthoimagery, acquired by drone photogrammetry over an outcrop area of 900 m^2, in the best exposed, central portion of the Moyagee fault (Figs. 4a–c; see also supplementary file A). Mapping shows that the metre-scale geometry of the fault array is similar to that mapped at regional scale (compare Figs. 4a and b): main fault segments are up to ~1–3.3 km-long, displaying an overall en-echelon arrangement. They are oriented ~10° clockwise with respect to the shear zone boundary, and are joined by shorter segments oriented ~15° counterclockwise from them (i.e. R- and P-type orientations, respectively, Figs. 3a, b and e). At any given scale, R-type shears consistently intersect S_{MT} at angles of 10°–25° clockwise. However, orientation data overlap when plotted for the entire area (compare Figs. 2a with 3c and 3d), masking the consistent angular relationship between S_{MT} and fault surfaces that is found at each occurrence of the geometry.

3.1.1 Brittle shear zones and veins

Fault segments comprise 1–10 cm-thick cataclasites showing dense networks of mm- to cm-thick dark tourmaline veins, containing a large proportion of gneiss clasts (i.e. up to 50%), which are typically millimetres to centimetres in size. Lateral veins branching off the main shear surfaces typically have millimetric to submillimetric thickness (Figs. 5a and b). Main fault segments commonly occur in paired shear systems (Figs. 4a–c, 5a–f) that are typically 0.5–1m apart, and are oriented at low-angles to S_{MT} in the host gneiss (Fig. 3). Paired brittle faults typically have main Y-shears joined by R-shears and subordinate P-shears, and flanked by evenly spaced, high-angle T-fractures (Figs. 5a–c). At least some of

the smaller-scale shear surfaces likely represent former high-angle T-fractures, attenuated during the subsequent ductile overprint that commonly focussed along the lithological contacts (Fig. 5a). Tourmaline-rich veins typically occur in dilatant sites and/or along principal slip surfaces (Fig. 5a). The volume of tourmaline veins associated with cataclasites increases in domains with more intense brecciation (compare Fig. 5b with Fig. 5f, which is likely representative of an incipient stage of fracturing). Notably, cataclasites and ultramylonites are tourmaline-free in places (Figs. 3a and 5g), and spatially associated with aplite and pegmatite veins. In the few cataclasites that completely escaped the subsequent ductile overprint (Figs. 5b–d), both foliation and lineation (S_{CAT} and L_{CAT}, respectively) are defined by the preferred orientation of granitic clasts in response to cataclastic flow. On horizontal exposures, foliated domains show R-, R'-, P-shears and T-fractures, shear bands and deflection of pre-existing foliation consistently indicate dextral shear sense (Figs. 5a–f). Some shears in R'-orientation (Fig. 5d) may have originated as tensile cracks that were subsequently reactivated as smaller-scale shears during post-rupture cataclastic flow.

Fault segments terminate in zones of complex fracturing a few metres wide, associated with horsetail splay systems (Figs. 5b–d), whose asymmetry with respect to the main fault surfaces agrees with the observed dextral displacement. Some fault segments include thicker veins (1–5 cm-thick, Fig. 5h), contain rare gneiss clasts (0.1–1cm in size) and have thicker lateral veins (up to 1 cm-thick), resembling injection veins of pseudotachylytes (Sibson, 1975; Swanson, 1988; Rowe et al., 2012; and references therein). Of special note are sharp fault contacts with tourmaline-filled periodic tensile fractures emanating from one side only (Figs. 5b and c).

3.1.2 Mylonites and ultramylonites

Most cataclasites are partially to completely overprinted by 1–50 cm-wide mylonites to ultramylonites. These ductile high-strain zones comprise SL tectonites with sub-vertical foliation (S_U, ultramylonite foliation) and prominent

horizontal stretching lineation (L_U), sub-parallel to S_{MT} and L_{MT} in the host gneiss, respectively (compare Figs. 2a and 3c). Mylonites are commonly paired with cataclasites in an arrangement where one side of a pre-existing cataclasite band preserves the dominantly brittle structures, whereas the other side exhibits a mylonitic foliation (Fig. 6). The high-strain ductile shear zones are very localized and the transition from cataclasite to ultramylonite is commonly sharp (Fig. 6). Elongate gneiss clasts with aspect ratio > 100:1 are common along the median zone of ultramylonites, defining a prominent compositional layering. On horizontal surfaces, sigmoidal clasts, S-C fabric and C' shear bands invariably indicate dextral shear sense (Figs. 5g, 6a and b). Veins at high-angle from the main fault surfaces are moderately to steeply north-dipping (S_{OBL}, foliation bearing an oblique stretching lineation, Fig.3d) and were commonly reactivated as reverse to oblique-slip ultramylonites. Stretching lineation associated with these shear zones (L_{OBL}) is at low angle from L_U (compare Figs. 3c and d).

3.1.3 Nucleation of shear fractures: the role of lithological contacts

External to the Moyagee fault, granitic gneiss typically contains a compositional layering formed of pegmatite and aplite veins oriented sub-parallel to S_{MT} (Fig. 7a). The common spatial association of cataclasites and aplites/pegmatites veins within the Moyagee fault (Figs. 5a, h and 7b–d) suggests that such lithological contacts were the preferred sites for cataclasite nucleation. The close spatial relationship between aplite/pegmatite veins and brittle structures is preserved even in the more common case of ductily sheared cataclasites (Fig. 7c), which locally occur along both sides of an aplite/pegmatite vein (Fig. 7d). Along the eastern margin of the Moyagee fault, pegmatite veins subparallel to S_{MT} show pinch-and-swell and boudinage structures, along en-echelon array of dextral C' shear bands (Fig. 7e and 7f). Here, C' shear bands are equally spaced (~7 cm apart), ~1–5 mm-thick and ~50 cm in length, centred on the sheared felsic vein. Each single shear band terminates ~20 cm away from the sheared pegmatite, by progressively rotating into parallelism with the gneissic foliation or by developing cm-long splays (Fig. 7f).

Some mylonitized cataclasites are not associated with tourmaline veins (Figs. 3a and 5g), but are localized within 10–20 cm thick felsic veins (Fig. 7g). These localized shear zones that can be followed for ~2 km along strike (stars in Fig. 3), display dextral offsets of a few metres (Fig. 7g) and may show knife-sharp boundaries against the host granitic gneiss (Fig. 7h). Importantly, such mylonitic veins, with or without their brittle precursor, are not visible in the other domains of the Cundimurra Shear Zone.

3.2 The Pinnacles fault

The Pinnacles fault is exposed at the northern tip of the Cundimurra Pluton (Fig. 2). At this locality, a network of granitic dykes is intruded into interlayered ultramafic schist and amphibolite of the greenstone belt adjacent to the Cundimurra Pluton (Fig. 8a). S_{MT} in the gneiss is truncated at a small angle by tourmaline-bearing cataclasites, similar to those exposed along the Moyagee fault. The gneiss-greenstone contact is marked by a ~1–3 m-thick quartz vein that pre-dates tourmaline-bearing cataclasites. The complete sequence across the contact is mylonitized, and a ~1 m-thick, tourmaline-bearing ultramylonitic cataclasite occurs along the western (pluton) side of the quartz vein (Fig. 8a). Within a ~15 m zone eastward from the quartz vein, mylonitic granite dykes were boudinaged within the less competent ultramafic schists and likewise show intense cataclasis/brecciation, associated with the introduction of tourmaline. This rupture zone contains angular fragments of mylonitic dykes and the mylonitic quartz vein (Figs. 8b–d). Millimetre-thick cataclasites, associated with emplacement of thin tourmaline-rich veins, are also found in other boudinaged dykes farther away from the granite-greenstone boundary (stars in Fig. 8a). On the greenstone side of the deformed intrusive contact, no tourmaline-bearing cataclasites were observed in either non-boudinaged granitic dykes or in host mafic to ultramafic gneiss and schist. Tourmaline veins locally show incipient domino-type boudinage (Fig. 8d; Goscombe and Passchier, 2003), suggesting that minor deformation occurred after vein emplacement.

3.3 The Golconda mylonite

North of the Moyagee fault, the Golconda mylonite (Fig. 2) contains granitic gneiss whose fabric exhibits geometry and kinematics identical to S_{MT} (compare insets a and b, Fig. 2). However, the main ductile fabric in the Golconda mylonite reflects accumulation of much larger amounts of strain than S_{MT}, evidenced by the prominent and pervasively developed C fabric (Fig. 9a). Moreover, field relationships indicate that the Golconda mylonite overprints cataclasites belonging to both the Moyagee fault and the Pinnacles fault (Fig. 2 and 3), and therefore postdates S_{MT}. This latter ductile deformation produced marked attenuation of both the host gneiss fabric and the cataclasite/ultramylonite zones of the Moyagee fault. Primary cataclasite structures are generally not preserved, but deformed versions are detectable as tourmaline-bearing ultramylonites. The various orientations of (Moyagee-related) Riedel fractures are rotated into parallelism with the mylonitic fabric, and mylonitic folds with subhorizontal axes and subvertical axial planes are common (Fig. 9b). Layered portions of ultramylonites locally record domino-type boudinage (Goscombe and Passchier, 2003) whose geometry is consistent with the generalized dextral shear sense observed in host, high-strain granitic gneiss (Fig. 9c).

The ductile fabric in the Golconda mylonite is in turn postdated by discrete, dextral strike-slip faults developed at a low angle to the prominent C fabric (Fig. 9d). Each of the main fault segments extend a few metres along strike in an en echelon arrangement and are linked by bridging (transfer) zones formed by closely spaced fracture surfaces (Fig. 9e). The major fault surfaces are oriented ~20° clockwise with respect to the primary C shear surfaces of the ductile fabric, i.e. an orientation kinematically analogous with R-type synthetic shears in brittle shear zones, with the ductile C orientation acting as Y-orientation at this scale. These faults offset the main C fabric and are interpreted to have nucleated along C surfaces, during the latter stages of slip. In Fig. 9d, right-stepping overlapping regions developed extensional oversteps with pinnate fractures (Figs. 9e and f). Observed displacement is about 1 m. Fault terminations show progressive rotation of fault surface towards parallelism with the main C fabric in host gneiss, with offset at fault tips accommodated by foliation-parallel slip. These faults

represent the youngest structures observed along the whole Lake Austin Shear Zone.

4 Microstructures

We use representative microstructures from three samples to support mesoscopic field observations. Although the study area clearly shows complex and protracted evolution, we selected samples that provide an adequate first-order assessment of the three main generations of fabrics across the northern portion of the CMSZ. Sample 219356, from a boudinaged pegmatite within granitic gneiss (Figs. 7e and f), is representative of the gneissic fabric predating the cataclasites. Sample 212762 contains a ~3 mm-thick cataclasite vein (developed at a high angle to S_{MT} in host granitic gneiss) that does not show any evidence of ductile overprint. Sample 212727 (section 4.3) represents a more evolved case containing a paired cataclasite-ultramylonite.

SEM (Scanning Electron Microscopy), EDS (energy dispersive spectroscopy) and EBSD (Electron Backscatter Diffraction, Prior et al., 1999) analysis of the ultramylonite was performed on polished XZ thin sections using a Jeol LV6610 SEM at the Electron Microscopy Centre, Plymouth University. Thin sections were chemically polished and carbon coated before acquisition of EBSD patterns. EBSD patterns were acquired with the following working conditions: 15 kV voltage, 70° sample tilt, working distance of 20 mm, and step size of 1.5 μm and 0.4 μm for polycrystalline quartz ribbons and ultrafine-grained tourmaline, respectively. Quartz crystallographic preferred orientation (CPO) of sample 198170, showing similar microstructures as sample 212727, was obtained using an automated fabric analyser microscope (G50-white; Peternell et al., 2010). For each pixel within the field of view, the G50 determines a unique orientation with a resolution of 43 μm/pixel. Afterwards, for each single quartz grain a mean c-axis orientation was selected with the freeware INVESTIGATOR software (Peternell et al., 2009).

4.1 Pre-cataclasite microstructures in granite gneiss

The salient microstructural features of S_{MT} are detailed in Zibra et al. (2014b), and are summarized here. Both plagioclase and K-feldspar show grain size reduction and overall evidence of deformation by low-temperature plasticity (Simpson, 1985), locally including microfractures and incipient core-and-mantle microstructure associated with albite + K-feldspar new grains (~2–20 μm in size). Recrystallized quartz grains are mostly in the 100–500 μm grain size range.

Sample 219356 is representative of the pinch-and-swell and boudinage structure developed along the boundaries between pegmatite veins and host granitic gneiss (Figs. 7e, 10a and B1). This sample recorded a domainal, bimodal microstructure. The granitic gneiss show incipient grain-size reduction, with mm-long lenses of recrystallized quartz aggregates wrapping around feldspar porphyroclasts. Lensoid quartz ribbons generally do not form along-strike continuous layers, and include aggregates of amoeboid to polygonal grains with grain size in ~100–500 μm interval, but with ~60–70% of grains clustering around 100–200 μm (Fig. 10b). Plagioclase and K-feldspar show comparable deformation features, with ≥80% of porphyroclasts showing evidence of incipient to widespread microfracturing (Figs. 10a and b), with both domino-type and shear band type fragmented porphyroclasts. In K-feldspar porphyroclasts, antithetic microfractures are mostly sub-parallel and equally spaced, suggesting that their development was crystallographically-controlled (Fig. 10b). Trails of feldspar aggregates (equant albite–oligoclase and orthoclase grains, 10–15 μm in size) coat microfractures and wrap around angular feldspar fragments (Fig. 10c). In striking contrast with such coarse-grained, protomylonitic foliation that typify the granitic gneiss, shear bands in C' orientation developed along the pegmatite margins (Figs. 7f and 10a) consist of mm-thick ultramylonite that sharply truncate S_{MT} (Fig. 10d). Ultramylonite contains aligned flakes of recrystallized biotite and muscovite, within an ultrafine matrix of equant feldspar (10–20 μm in size) and lensoid quartz ribbons (grain size: 50–100 μm).

4.2 Cataclasites

The cataclasite (sample 212762, Figs. 10e–h and Supplementary Materials B2) is from a lateral vein branching off at high-angle from a main fault surface. Microstructural features of the pre-cataclasite gneissic foliation (S_{MT}) in this sample are comparable to those described in the previous section. The background fabric is truncated by a ~3 mm-thick, dark cataclasite vein, developed at ~45° from S_{MT} (Fig. 10e). The vein shows irregular margins and locally contains large, anhedral tourmaline$_1$ grains (up to 2–3 mm in size), set within a fine-grained matrix mainly composed of tourmaline$_2$, muscovite, biotite, opaque phases and angular to rounded clasts of the host gneiss (Fig. 10f). Tourmaline$_2$ occur as ~5–100 μm euhedral and randomly-oriented grains that completely pseudomorphosed tourmaline$_1$, largely overgrowing other phases in the vein matrix. Lateral veins departing from the main cataclasite are ~10–100 μm thick and are associated with intensely developed fractures in both quartz and feldspars in the host gneiss. The portion of granitic gneiss flanking the cataclasite contains ultramylonite layers composed of completely recrystallized feldspar (10–20 μm in size) and lensoid quartz ribbons containing polygonal, strain free grains (Figs. 10f, g and B2). Angular clasts of ultramylonite occur within the cataclasite, and thin, tourmaline-bearing cataclasite veins, branching off the main surface, postdate ultramylonite (Figs. 10g and h).

4.3. Ultramylonites

The ultramylonite sample 212727 (Figs. 6b and 11a) is representative of paired, tourmaline-bearing cataclasites-ultramylonites. The eastern side of the shear zone preserves cataclastic microstructures, and includes a dense network of veins both sub-parallel and at high angle to the main vein, containing angular fragments of host gneiss, ranging in size from a few μm to several mm. The mineral assemblage of these veins is comparable to that of the cataclasite (sample 212762). Even veins that are at a high angle (30–50°) to the main vein are locally overprinted by mylonitic deformation and show elongated polycrystalline quartz ribbons wrapped by the tourmaline-rich matrix (Fig. 11b). Feldspar and quartz in the damage zone flanking the veins are dissected along a network of fractures ranging in width from a few microns to ~100 μm.

The opposing western side of the main tourmaline-bearing vein is overprinted by a cm-thick ductile shear zone. The margin of the vein is moderately deformed and most gneiss clasts within the vein have acquired a sigmoidal shape or have long axes inclined to the vein margin, in agreement with the dextral shear sense observable at outcrop scale. The transition from mylonite, near the margin of the vein, to ultramylonite occurs over ~2 mm. The mylonite layer contains σ-shaped feldspar porphyroclasts, up to ~400 μm in size, set in a fine-grained matrix composed of recrystallized feldspar, quartz, muscovite and $tourmaline_2$. Lensoid quartz ribbons are several millimetres long and typically one-grain thick, and quartz grains are ~40–200 μm in size. Feldspar porphyroclasts show patchy undulose extinction and microfractures and are wrapped by aggregates of albite–oligoclase and orthoclase equant grains, ~10–20 μm in size. Transposed T_1 veins contain boudinaged $tourmaline_1$ porphyroclasts and ultrafine $tourmaline_2$ aggregates (grain size: <<1–10 μm) aligned sub-parallel to S_U. Here, most feldspar porphyroclasts show synthetic microfractures (i.e. shear band type clasts, Fig. 11c).

In the centre of the ductile shear zone, the transition to the ~1 cm-thick ultramylonite layer occurs through gradual disappearance of feldspar porphyroclasts and through an increase in transposed tourmaline veins (Figs. 11d and e). The one-grain thick quartz ribbons at the mylonite-ultramylonite transition as well as within the ultramylonites contain nearly equant quartz grains, 30–50 μm in size, and show pinch-and-swell and boudinage microstructures, with boudin neck filled by K-feldspar (Figs. 11d–f). The ultramylonite matrix is dominated by ultrafine-grained $tourmaline_2$ (grain size: <1–20 μm, Fig. 11g) and contains also equant quartz and feldspar grains with dispersed biotite and muscovite flakes of comparable size. In places, euhedral $tourmaline_2$ crystals are concentrated in microlayers, defining a compositional layering parallel to S_U (Figs. 11h and i). Ultramylonites locally contain elongate quartz grains and opaque aggregates up to 1 mm in size aligned parallel to incipient shear bands (Fig. 11i). A similar microstructure is described in Menegon et al. (2015), in a monzonite ultramylonite from Lofoten, northern Norway.

The c-axes of quartz grains in the monomineralic, polycrystalline, 20–100 μm thick ribbons in the ultramylonite (e.g. Figs. 11d and g) define a crossed-girdle fabric (Lister, 1977) with an opening angle of ~70–75° (Fig. 12a), suggesting maximum deformation temperature of ~600 ± 50°C (fig. 2 in Law, 2014). The a-axes have a maximum at low angle to the stretching lineation, and the poles to the prism- and rhomb planes have maxima subparallel to the foliation.

Tourmaline grains in the ultramylonite matrix are preferentially elongated at ~30° from the trace of the ultramylonite boundary, measured anticlockwise. This defines a strong shape-preferred orientation (SPO) consistent with the dextral shear sense the sample (Fig. 12b). Tourmaline grains are preferentially oriented with their c-axis subparallel to the stretching lineation and with the poles to the prism planes distributed on a girdle parallel to the YZ plane of finite strain ellipsoid (Fig. 12c). Low-angle boundaries (misorientation: 2°–10°) are scarce and preferentially occur in relatively large grains (10–20 μm in length, Fig. 12b).

Microstructures from the Golconda mylonite are similar to those in the cataclasite-derived ultramylonites.

5 Discussion

5.1 The Moyagee and Pinnacles faults. Localization of brittle rupture along ductile precursors

5.1.1 Localization of shear deformation at lithological boundaries

The ~7 km-long Moyagee fault forms an en echelon array of overstepping, dextral R-type shears (~1–3 km-long) joined by shorter, synthetic P-orientation shears (~0.5 km-long, Fig. 3a and b; Ahlgren, 2001 and references therein). This geometry is repeated from map-scale down to the sub-metric scale (Figs. 4a–d. See also plates 1–4 in appendix A). Observations from the margins of the fault network indicate that lithological boundaries between felsic veins and host granitic gneiss commonly exhibit more intense pre-cataclasite fabrics than within the volume of adjacent lithologies (Figs. 7e and f, 10a–d and B1). In fact, we show

453 that, before the development of the Moyagee and Pinnacles faults, lithological
454 contacts recorded very heterogeneous strain. Shearing within the granitic gneiss
455 was accommodated by widespread recrystallization and dislocation creep in the
456 weaker quartz layers, while plagioclase and K-feldspar experienced widespread
457 fracturing in combination with fine-grained recrystallization (Figs. 10b and c).
458 Notably, microstructures show that quartz lenses did not coalesce to develop an
459 along-strike interconnected network of ribbons (Figs. 10b and Supplementary
460 Materials B1), suggesting that the rheology of the "strong" feldspar porphyroclasts
461 played a major role in controlling the bulk rheology of the granitic aggregate,
462 because a load-bearing framework of strong phases existed (Handy, 1990). In
463 contrast, lithological contacts between felsic veins and host gneiss were clearly
464 the sites of dramatic strain softening and were the loci for the development of
465 ultramylonites dominated by ultrafine feldspar (10–50 μm in size) and syntectonic
466 biotite and muscovite flakes (Fig. 10d and Supplementary Materials B1).
467 We propose that lithological boundaries between felsic veins and host granite
468 gneiss preferentially concentrated strain, similar to what is typically observed in
469 many other granitoids (e.g. (White, 1996, 2012; Pennacchioni and Mancktelow,
470 2007) and at bimechanical interfaces in other lithologies (White, 2003; Kelemen
471 and Hirth, 2007). This behaviour would have occurred by a combination of strain
472 hardening along the bi-material interface, and a consequent increase and
473 enhanced heterogeneity in the stress/strain rate distribution that in turn drove the
474 textural changes that resulted in weakening and strain localization.

475 ### 5.1.2 Deformation overprinting
476
477 Along the Moyagee fault, abundant evidence that these same lithological
478 boundaries later became the preferred sites of cataclasite nucleation on discrete
479 rupture surfaces (Fig. 13a). Microstructures from non-mylonitized cataclasite (Fig.
480 10e–h and Supplementary Materials B2) show that pre-cataclasite ultramylonite
481 layers might have played a key role in controlling the nucleation of brittle
482 structures. Several studies indicate that ductile strain localization in granitic rocks
483 can be strongly controlled by pre-existing planar heterogeneities, lithological
484 boundaries and brittle precursor structures (Mancktelow and Pennacchioni, 2005;
485 Pennacchioni and Mancktelow, 2007; Pennacchioni and Zucchi, 2013). In

contrast, pre-existing ductile shear zones and lithological boundaries do not necessarily control the nucleation of brittle faults in granitoids, and are often cut, even at a very low angle, by subsequent fractures and faults (e.g., Pennacchioni and Mancktelow, 2013). In contrast, the Moyagee fault represents a case where cataclasites formed in an otherwise ductile regime, were spatially and temporally coeval with ductile strain concentrations and were subsequently mylonitized. This outcome suggests that a transient rheological behaviour, and not only the geometry of precursor structures, played an important role in the generation of cataclasites along the Moyagee fault (White, 1996, 2003, 2004, 2005, 2012; Kelemen and Hirth, 2007; Stewart and Miranda, 2017).

The transition from dominantly ductile to brittle deformation may require the development of ductile fractures (Weinberg and Regenauer-Lieb, 2010). Coalescence of microvoids generated via intergranular fracturing, during deformation of feldspar in the brittle–ductile transition, can lead to development of rupture zones focussed in domains characterized by strong plastic deformation (Shigematsu et al., 2004). The process of ductile fracturing may account for the nucleation of the brittle structures described in this paper.

Brittle structures in granitic gneiss of the Pinnacles fault are similar to those observed along the Moyagee fault. The greenstone portion of this fault segment shows that tourmaline-bearing cataclasite only developed where the competent granite dykes were boudinaged within the weak schistose matrix (Figs. 8a–c). As for the Moyagee fault, syntectonic dilatancy generated during dyke boudinage enabled emplacement of tourmaline-rich fluids.

5.1.3 Occurrence of dynamic rupture

Evidence for seismic rupture resides in the tensile fractures that form asymmetrically on one side of a primary shear plane. Other studies have shown that these periodic arrays are a product of dynamic rupture propagation (Di Toro et al., 2005; Griffith et al., 2009; Rowe and Griffith, 2015 and references therein). The preservation of these often-delicate structures highlights the high-degree of preservation of the complete fault history. The infilling of these fractures by tourmaline enhances their outward similarity with pseudotachylyte-filled fractures (Fig. 5c), and is consistent with the simultaneous to near-simultaneous formation

519 of rupture and veins. However, we must note that, in the case described by Di
520 Toro et al. (2005), pseudotachylyte veins provided an independent evidence for
521 slip at seismic slip rates. On the other hand, recent studies show that
522 pseudotachylyte is no longer considered the only indicator of fossilized
523 earthquake ruptures (Rowe and Griffith, 2015). Consequently, the fault network
524 studied here contains paleoseismic record of the oldest earthquakes yet
525 documented on Earth. We infer that evidence for dynamic rupture is only rarely
526 preserved along the LASZ (Fig. 5c) since the indicative features are mostly
527 masked by both cataclasites and ultramylonites (Fig. 13).
528 Any positive feedback between strain hardening along lithological boundaries, a
529 consequent increase and enhanced heterogeneity in the stress distribution, in turn
530 driving the textural changes that resulted in weakening and strain localization,
531 may have produced greatly enhanced strain rate. This behaviour in turn may have
532 culminated in shear rupture at the relatively high temperature (~600 ± 50°C) that
533 prevailed during the development of the main brittle-then ductile structures in the
534 study area. There need not be a direct path from ductile-to-brittle shear, and
535 cataclasites may have simply developed at mechanical anisotropies (C-surfaces)
536 associated with ductile strain concentration (Shigematsu et al., 2004). However,
537 direct transition through ductile rupture is not precluded. Notwithstanding the
538 evidence for initial seismic rupture, the transition to cataclasis and ductile shear
539 points to aseismic slip along the weak discontinuity, i.e. the initial rupture surface.

540 Although tourmaline veins typically demarcate the zones of localized deformation,
541 both discrete shear fractures and high-strain zones are not always associated with
542 such veins (Figs. 3, 5g, 7g and h). In the first instance, tourmaline introduction
543 appears to be associated with dilatancy during brittle failure (i.e. compare Figs. 5a
544 and b). Although fluid pressure would have played a role, we interpret the
545 fractures to be stress-driven, as opposed to fluid-pressure-driven (Cox and
546 Munroe, 2016), given the similarity of barren and tourmaline-bearing shear
547 fractures. This interpretation is consistent with the presence of systematic arrays
548 of synthetic R- and P-shears, which represent the typical geometric arrangement
549 of synthetic-driven Riedel shear zones, predicted by classical failure models (Figs.
550 2 and 3; Tchalenko and Ambraseys, 1970). Therefore, we conclude that
551 tourmaline-rich fluids were “passively” emplaced in dilational sites during brittle

552 shearing. Therefore, while the contribution of fluid pressure cannot be excluded
553 from triggering rupture, in this case we consider it unlikely to have played a
554 dominant role in the ductile-to-brittle transition.

555

556 5.2 Evolution of the Lake Austin Shear Zone

557

558 Field and microstructural evidence indicate that most ultramylonites exploited pre-
559 existing faults with cataclasites, which is best expressed in partial overprinting (i.e.
560 paired cataclasites-ultramylonites, Figs. 5g, 6a, b and 11a) and tourmaline-
561 bearing, layered ultramylonites (Figs. 7c, d, 9b and c). For complete ductile
562 overprints, evidence for the cataclasite precursors is preserved as tourmaline-
563 bearing, layered ultramylonites and attenuated, tourmaline-bearing T-fractures
564 (Figs. 6a and b, 7c, d, 9b and c). Brittle fault segments showing limited cataclasis
565 and small volumes of tourmaline-rich veins may represent brittle structures that
566 experienced insufficient deformation to become fully developed, while greater
567 accumulated brittle displacement was likely associated with the emplacement of
568 larger volumes of tourmaline (compare Figs. 5a and b). In both the Moyagee and
569 Pinnacles faults, cataclasite-derived ultramylonites show the same kinematics as
570 the solid-state deformation recorded within the Cundimurra Shear Zone (S_{MT},
571 compare Figs. 2a, 3c, 8a and 13). In these areas, deformation was extremely
572 heterogeneous, so that granitic gneiss flanking ultramylonites retain their pre-
573 cataclasite, homogeneous gneissic foliation (S_{MT}, e.g. Fig. 7h). Both faults with
574 their brittle-then-ductile heterogeneous shear are overprinted by ductile structures
575 along the Golconda mylonite, i.e. a 4 km-wide high-strain zone marked by
576 homogeneous fabric and prominent C-orientation shear bands (Fig. 9a).

577 We therefore propose the following multi-step evolution (Fig. 13) for the
578 subsolidus structural evolution of the CMSZ. After pluton crystallization,
579 subsolidus fabrics developed at high- and then moderate-temperature (S_{HT} and
580 S_{MT}, respectively, Zibra et al., 2014b), during progressive cooling. The switch from
581 S_{HT} to S_{MT} reflects a major rheological transition in feldspar, from steady-state
582 dislocation creep to low-temperature plasticity (based on a comparison of coarse

583 grains with interlobate boundaries and undulose extinction in Fig. 14c of Zibra et
584 al. (2014b) with the observation of finer, equant grains in mixed polyphase arrays
585 in Fig. 15b in Zibra et al. (2014b). Such a transition is anticipated to enhance
586 competency contrast between pegmatites/aplite veins and host gneiss, promoting
587 a transition, either directly or as preferred sites for stress heterogeneity, to seismic
588 rupture and cataclasis (Figs. 7e, f and 13a), which eventually led to the
589 development of km-scale brittle shear zone networks (i.e. Moyagee and Pinnacles
590 faults, Fig. 13b) in Riedel orientations (~parallel to C-surfaces) relative to the
591 regional shear zone boundary (Figs. 3a and b). Extensive fracturing of feldspar
592 promoting the formation of fine-grained C- and C' bands that subsequently
593 localized ultramylonitic deformation in granitoid mylonites was described by
594 Viegas et al. (2016). The substantive change in material properties triggered by
595 cataclasis and introduction of tourmaline, with no change in external conditions
596 (i.e. *P* and *T*), produced ultramylonites at the expenses of cataclasites (Figs. 6a
597 and b).

598 The tendency for reversion to ductile deformation reflects: (1) the combined
599 softening effect produced by faulting and grain-size reduction; plus (2) the overall
600 conditions in the Golconda mylonite region that supported bulk ductile shear
601 through the development of the penetrative S/C fabric. Several studies of
602 deformation at the frictional-viscous transition in the granitoid middle crust have
603 consistently concluded that the main rheological effect of brittle grain-size
604 reduction is to activate grain-size sensitive creep in the resulting fine-grained
605 material during viscous deformation (Fitz Gerald and Stünitz, 1993; Fusseis and
606 Handy, 2008; Viegas et al., 2016; Wehrens et al., 2016). Likewise, we interpret
607 the strong shape- and crystallographic preferred orientation of tourmaline in the
608 ultramylonites ([001] parallel to elongation of grains and to stretching lineation) as
609 the result of oriented grain growth coupled with grain rotation during diffusion
610 creep (Bons and den Brok, 2000; Getsinger and Hirth, 2014; Negrini et al., 2014).
611 This interpretation is supported by the lack of low-angle boundaries in the
612 tourmaline grains, with a very few exceptions (Fig. 12b), which indicates that the
613 grains are essentially strain free. Thus, the ultrafine-grained tourmaline-rich
614 mixture represented the rheological weak phase of the ultramylonite, whereas
615 monomineralic quartz ribbons deforming by dislocation creep were clearly

616 stronger because they underwent boudinage and pinch-and-swell (Figs. 11e–g).
617 This observation is in line with recent studies, which highlight that although quartz
618 deforming by dislocation creep is commonly assumed to represent the weak
619 phase controlling the rheology of the middle crust, fine-grained polyphase
620 mixtures typically found in ultramylonites are weaker than quartz and deform at
621 faster strain rates than monomineralic quartz domains (Kilian et al., 2011; Platt,
622 2015; Viegas et al., 2016).

623 The transition from localized (Moyagee and Pinnacles faults) towards diffuse
624 (Golconda mylonite) deformation (Fig. 13c) might simply have resulted from the
625 coalescence of ductile shear strain during progressive deformation. An
626 anastomosing network of narrow shear zones is anticipated to accommodate
627 limited amounts of finite displacement on each strand; volumetrically large
628 distributed strains would be attained through broadening of the deforming zone,
629 which eventually evolve into a zone of more distributed deformation (White, 1996;
630 Mancktelow, 2002; Pennacchioni and Mancktelow, 2007; Menegon and
631 Pennacchioni, 2010).

632 In summary, the simple generation of transient brittle discontinuities within a
633 continuously active ductile shear zone was concentrated in the region of the
634 Golconda mylonite and the resulting weakening induced by the grain-size
635 reduction could explain the ductile-brittle-ductile overprint relationships. The
636 structural evolution that we infer is consistent with continuous syndeformational
637 emplacement and cooling such that all fabrics of any given stage exhibit invariable
638 kinematics (Fig. 13d).

639

640 5.3 Deformation framework and the role of emplacement-related
641 structures

642

643 The dominant deformation mode during the syntectonic emplacement of the
644 Cundimurra pluton is one of viscous flow that occurred during both for the earliest
645 magmatic (Zibra et al., 2014b) and later dominant solid-state fabrics. The
646 distinctive fabric elements in order of formation are: magmatic flow foliations

(compositional layering including shear band structures); solid-state deformation producing the background S_{MT} and oblique C-surfaces (shear bands); cataclasites that disrupt S_{MT}; mylonites and ultramylonites that form on pre-existing cataclasites; and a high-strain analogue of S_{MT} (the Golconda mylonite) with pervasive C-surface development that overprints S_{MT} and the localized cataclasite/ultramylonite zones. Lastly, the latter high strain zone is itself subject to faulting (Figs. 9d–f). This sequence is clearly an example of emplacement concomitant with deformation, where deformation outlasted pluton crystallization.

A striking aspect of the LASZ is the monotonic nature of its kinematic evolution, from magmatic flow stage through solid-state deformation and transient brittle rupture (Fig. 13). The basic components of this history are an effectively constant granitoid composition, syndeformational cooling and a fixed movement picture, which includes dextral displacement. The nature and intensity of fabrics observed are a function of finite strain intensity and mode of deformation. Ductile fabrics exhibit S-C fabrics with the intensity and spacing of C-planes varying with finite strain. The obliquity of the C-surface to the shear zone boundary, as defined by regional lithological boundaries, is commonly used to denote it as the C' orientation, though its formation in this orientation is simply the result of the bulk triclinic kinematics (Lister and Snoke, 1984; Jiang and White, 1995). The primary shear direction lies within the C-surfaces and parallel its intersection with the sectional vorticity normal plane, consistent with the orientation of the stretching lineations recorded throughout the area (e.g. Figs. 2 and 3).

Brittle behaviour was transient, being preceded and followed by the dominant viscous deformation in all instances (e.g. Fig. 9a–c) but the last deformation stage (Figs. 9d–f). Decreasing temperature, increasingly heterogeneous bulk fabric and microstructural changes may have induced strain rate/stress changes, leading to the transient brittle behaviour. Brittle rupture nucleated in this ductile volume as a function of ductile flow (Weinberg and Regenauer-Lieb, 2010), rather than propagating into the volume from out of a more brittle volume above that is often found to be the case in other deforming rock volumes near the crustal brittle-ductile transition. Thus, the observed structures are a continuum of behaviour that reflects transient temporal and spatial partitioning of strain rate and strain.

679 Brittle behaviour within the CMSZ was transient, with transition from and reversion
680 to dominantly viscous deformation (e.g. Fig. 9a–c) in all but the last deformation
681 stage (Figs. 9d–f); that is, ductile flow was the precursor state for nucleation of
682 brittle rupture within the CMSZ (e.g. Weinberg and Regenauer-Lieb, 2010). That
683 the brittle faults formed within an ambient ductile regime is demonstrated by their
684 overprint by ductile deformation on a regional scale. The ductile-brittle-ductile
685 transition was a local, transient change in rheological response, rather than the
686 result of gross changes in crustal conditions. The variations in parameters such as
687 temperature (decreasing), bulk fabric (increasingly heterogeneous) and
688 microstructure (generally finer grained, more deformed) during shear zone
689 evolution necessarily influenced the rheological response through their control of
690 micromechanical processes. In turn, the feedback among such processes (e.g.
691 Kelemen and Hirth, 2007) may have induced strain rate/stress variations,
692 amplified in the absence of dampening conditions that would have produced
693 uniform, steady-state flow. The heterogeneity of micro- and macro-structures
694 argues against uniform behaviour, despite the long-term consistency of the
695 kinematic framework. Instead, the observed structures (foliated granitoids,
696 mylonites, shear fractures) form a continuum that reflects secular partitioning of
697 strain rate, and necessarily strain, as a result of intrinsic lithological
698 heterogeneities, such as aplite and pegmatite dykes, within the granitic body.

699 Two first-order features, established during pluton emplacement, played a major
700 role in controlling the subsolidus evolution of the cooling pluton. Firstly, the
701 Cundimurra Pluton/shear zone is a ~185 km-long, wedge-shaped body, varying in
702 width from a maximum of ~30 km in its southern portion, to a minimum of less
703 than 3 km near its northern domain (Figs. 1b and 2). Secondly, initial melt-induced
704 strain partitioning confined the strike-slip component of shearing within the pluton
705 (Fig. 1c; compare also orientation data for granitic gneiss and greenstones, Fig. 2,
706 insets a and c, respectively). Strain partitioning persisted during subsolidus
707 deformation, so that no visible strike-slip-related structures developed in the
708 greenstone component of the CMSZ, neither during pluton emplacement nor
709 retrograde shearing (Zibra et al., 2014b). These factors likely account for the
710 development of the Lake Austin Shear Zone in the narrowest segment of the
711 Cundimurra pluton/shear zone (Fig. 2). Bulk shear strain rate across a shear zone

712 is defined as the ratio between the particle velocity (v) and the shear zone width
713 (w). If boundary conditions maintained an approximately constant velocity, then a
714 decrease in width of the accommodation zone would have required a local
715 increase in strain rate in the LASZ portion of the CMSZ. Heterogeneous
716 partitioning of the strain rate, potentially with local fluctuations, may have in turn
717 have triggered the onset of brittle deformation at relatively high temperature.

718

719 6 Conclusions

720

721 This study examines the multistage evolution of the large-scale and long-lived
722 Cundimurra Shear Zone. During the syn-magmatic stages, transpressional
723 deformation was accommodated within a broad high-strain zone (>200 km in
724 length and 3–30 km in width), where the syntectonic Cundimurra pluton
725 partitioned the dextral slip component of shearing. With the cessation of
726 magmatism, syndeformational cooling of the shear zone induced dramatic strain
727 concentration in the narrowest portion of the pluton, where the superposed
728 generations of structures document the cyclical transition from dominantly ductile
729 to brittle behaviour. This study suggests that transient ductile instabilities
730 established along lithological boundaries culminated in seismic shear rupture at
731 relatively high temperature (~500°C). Our study therefore supports the view that
732 local heterogeneities (mainly pegmatites, aplite veins, and synkinematic
733 cataclasites formed in an overall ductile deformation regime) played an important
734 role in controlling nucleation and development of subsolidus high-strain zones.
735 Just as importantly, this work suggests that the regional (i.e. $10–10^2$ km)
736 architecture established during pluton emplacement, in the form of shape and
737 width of the pluton/shear zone, and the regime of strain partitioning, induced by
738 melt-present deformation, played a key role in controlling the local distribution of
739 brittle and then ductile subsolidus structures.

740

Acknowledgements

We thank Virginia Toy and Federico Farina for very helpful and constructive reviews that substantially improved the clarity of this contribution. We also thank the Editor William M. Dunne for prompt handling of the manuscript and for the additional, very careful and constructive review of the second version of this paper. M. Prause and M. Jones helped in preparing the figures. P. Vota, T. Zama and D. Twist provided invaluable support during fieldwork. This work benefited from numerous field discussions with J.H. Kruhl, A. Ord, C. Passchier, M. Peternell, S. Piazolo and R. Weinberg. We thank them all. JCW was supported by a NSERC Canada Discovery Grant. LM was supported by an FP7 Marie Curie Career Integration Grant (grant agreement PCIG13-GA-2013-618289). The staff at the Plymouth University Electron Microscopy Centre is thanked for support during SEM analysis. The paper is published with the permission of the executive director of the Geological Survey of Western Australia.

References

Ahlgren, S.G., 2001. The nucleation and evolution of Riedel shear zones as deformation bands in porous sandstone. Journal of Structural Geology 23, 1203–1214. https://doi.org/10.1016/S0191-8141(00)00183-8

Blanquat, M. de Saint, Horsman, E., Habert, G., Morgan, S., Vanderhaeghe, O., Law, R., Tikoff, B., 2011. Multiscale magmatic cyclicity, duration of pluton construction, and the paradoxical relationship between tectonism and plutonism in continental arcs. Tectonophysics 500, 20–33. https://doi.org/10.1016/j.tecto.2009.12.009

Bons, P.D., den Brok, B., 2000. Crystallographic preferred orientation development by dissolution–precipitation creep. Journal of Structural Geology 22, 1713–1722. https://doi.org/10.1016/S0191-8141(00)00075-4

Cassidy, K., Champion, D., Krapez, B., Barley, M., 2006. A revised geological framework for the Yilgarn Craton, Western Australia, Geological Survey of Western Australia, Record 8(8).

Christensen, N.I., Mooney, W.D., 1995. Seismic velocity structure and composition of the continental crust: A global view. Journal of Geophysical

772 Research: Solid Earth 100, 9761–9788. https://doi.org/10.1029/95JB00259
773 Christiansen, P.P., Pollard, D.D., 1997. Nucleation, growth and structural
774 development of mylonitic shear zones in granitic rock. Journal of Structural
775 Geology 19, 1159–1172. https://doi.org/10.1016/S0191-8141(97)00025-4
776 Cox, S.F., Munroe, S.M., 2016. Breccia formation by particle fluidization in fault
777 zones: Implications for transitory, rupture-controlled fluid flow regimes in
778 hydrothermal systems. American Journal of Science 316, 241–278.
779 https://doi.org/10.2475/03.2016.02
780 Crider, J.G., 2015. The initiation of brittle faults in crystalline rock., Journal of
781 Structural Geology. https://doi.org/10.1016/j.jsg.2015.05.001
782 Di Toro, G., Nielsen, S., Pennacchioni, G., 2005. Earthquake rupture dynamics
783 frozen in exhumed ancient faults. Nature 436, 1009–1012.
784 https://doi.org/10.1038/nature03910
785 Fitz Gerald, J.D., Stünitz, H., 1993. Deformation of granitoids at low metamorphic
786 grade. I: Reactions and grain size reduction. Tectonophysics 221, 269–297.
787 https://doi.org/10.1016/0040-1951(93)90163-E
788 Fusseis, F., Handy, M.R., 2008. Micromechanisms of shear zone propagation at
789 the brittle–viscous transition. Journal of Structural Geology 30, 1242–1253.
790 https://doi.org/10.1016/j.jsg.2008.06.005
791 Getsinger, A.J., Hirth, G., 2014. Amphibole fabric formation during diffusion creep
792 and the rheology of shear zones. Geology 42, 535–538.
793 https://doi.org/10.1130/G35327.1
794 Goleby, B.R., Blewett, R.S., Korsch, R.J., Champion, D.C., Cassidy, K.F., Jones,
795 L.E.A., Groenewald, P.B., Henson, P., 2004. Deep seismic reflection profiling
796 in the Archaean northeastern Yilgarn Craton, Western Australia: implications
797 for crustal architecture and mineral potential. Tectonophysics 388, 119–133.
798 https://doi.org/10.1016/j.tecto.2004.04.032
799 Goncalves, P., Poilvet, J.C., Oliot, E., Trap, P., Marquer, D., 2016. How does
800 shear zone nucleate? An example from the Suretta nappe (Swiss Eastern
801 Alps). Journal of Structural Geology 86, 166–180.
802 https://doi.org/10.1016/j.jsg.2016.02.015
803 Goscombe, B.D., Passchier, C.W., 2003. Asymmetric boudins as shear sense
804 indicators—an assessment from field data. Journal of Structural Geology 25,
805 575–589. https://doi.org/10.1016/S0191-8141(02)00045-7

806 Griffith, W.A., Rosakis, A., Pollard, D.D., Ko, C.W., 2009. Dynamic rupture
807 experiments elucidate tensile crack development during propagating
808 earthquake ruptures. Geology 37, 795–798.
809 https://doi.org/10.1130/G30064A.1
810 Guermani, A., Pennacchioni, G., 1998. Brittle precursors of plastic deformation in
811 a granite: an example from the Mont Blanc massif (Helvetic, western Alps).
812 Journal of Structural Geology 20, 135–148. https://doi.org/10.1016/S0191-
813 8141(97)00080-1
814 Handy, M.R., 1990. The solid-state flow of polymineralic rocks. Journal of
815 Geophysical Research 95, 8647–8661.
816 https://doi.org/10.1029/JB095iB06p08647
817 Hobbs, B., Mühlhaus, H., Ord, A., 1990. Instability, softening and localization of
818 deformation. Geological Society, London, Special Publications 54, 143–165.
819 Jaquet, Y., Schmalholz, S.M., 2017. Spontaneous ductile crustal shear zone
820 formation by thermal softening and related stress, temperature and strain rate
821 evolution. Tectonophysics. https://doi.org/10.1016/j.tecto.2017.01.012
822 Jiang, D., White, J.C., 1995. Kinematics of rock flow and the interpretation of
823 geological structures, with particular reference to shear zones. Journal of
824 Structural Geology 17, 1249–1265. https://doi.org/10.1016/0191-
825 8141(95)00026-A
826 Kelemen, P.B., Hirth, G., 2007. A periodic shear-heating mechanism for
827 intermediate-depth earthquakes in the mantle. Nature 446, 787–790.
828 https://doi.org/10.1038/nature05717
829 Kilian, R., Heilbronner, R., Stünitz, H., 2011. Quartz grain size reduction in a
830 granitoid rock and the transition from dislocation to diffusion creep. Journal of
831 Structural Geology 33, 1265–1284. https://doi.org/10.1016/j.jsg.2011.05.004
832 Kretz, R., 1983. Symbols for rock-forming minerals. American Mineralogist 68,
833 277–279.
834 Law, R.D., 2014. Deformation thermometry based on quartz c-axis fabrics and
835 recrystallization microstructures: A review., Journal of Structural Geology.
836 https://doi.org/10.1016/j.jsg.2014.05.023
837 Lister, G., Snoke, A., 1984. S-C Mylonites. Journal of Structural Geology 6, 617–
838 638. https://doi.org/10.1016/0191-8141(84)90001-4
839 Mancktelow, N.S., 2002. Finite-element modelling of shear zone development in

viscoelastic materials and its implications for localisation of partial melting. Journal of Structural Geology 24, 1045–1053. https://doi.org/10.1016/S0191-8141(01)00090-6

Mancktelow, N.S., Pennacchioni, G., 2005. The control of precursor brittle fracture and fluid–rock interaction on the development of single and paired ductile shear zones. Journal of Structural Geology 27, 645–661. https://doi.org/10.1016/j.jsg.2004.12.001

Menegon, L., Fusseis, F., Stunitz, H., Xiao, X., 2015. Creep cavitation bands control porosity and fluid flow in lower crustal shear zones. Geology 43, 227–230. https://doi.org/10.1130/G36307.1

Menegon, L., Pennacchioni, G., 2010. Local shear zone pattern and bulk deformation in the Gran Paradiso metagranite (NW Italian Alps). International Journal of Earth Sciences 99, 1805–1825. https://doi.org/10.1007/s00531-009-0485-6

Myers, J.S., 1995. The generation and assembly of an Archaean supercontinent: evidence from the Yilgarn craton, Western Australia. Geological Society, London, Special Publications 95, 143–154. https://doi.org/10.1144/GSL.SP.1995.095.01.09

Negrini, M., Stünitz, H., Nasipuri, P., Menegon, L., Morales, L.F.G., 2014. Semibrittle deformation and partial melting of perthitic K-feldspar: An experimental study. Journal of Geophysical Research: Solid Earth 119, 3478–3502. https://doi.org/10.1002/2013JB010573

Pennacchioni, G., Mancktelow, N., 2007. Nucleation and initial growth of a shear zone network within compositionally and structurally heterogeneous granitoids under amphibolite facies conditions. Journal of Structural Geology 29, 1757–1780.

Pennacchioni, G., Zucchi, E., 2013. High temperature fracturing and ductile deformation during cooling of a pluton: The Lake Edison granodiorite (Sierra Nevada batholith, California). Journal of Structural Geology 50, 54–81. https://doi.org/10.1016/j.jsg.2012.06.001

Peternell, M., Hasalová, P., Wilson, C.J.L., Piazolo, S., Schulmann, K., 2010. Evaluating quartz crystallographic preferred orientations and the role of deformation partitioning using EBSD and fabric analyser techniques. Journal of Structural Geology 32, 803–817.

Peternell, M., Kohlmann, F., Wilson, C.J.L.C., Seiler, C., Gleadow, A.J.W., 2009. A new approach to crystallographic orientation measurement for apatite fission track analysis: effects of crystal morphology and implications for automation. Chemical Geology 265, 527–539. https://doi.org/10.1016/j.chemgeo.2009.05.021

Platt, J.P., 2015. Influence of shear heating on microstructurally defined plate boundary shear zones. Journal of Structural Geology 79, 80–89. https://doi.org/10.1016/j.jsg.2015.07.009

Prior, D.J., Boyle, A.P., Brenker, F., Cheadle, M.C., Day, A., Lopez, G., Peruzzi, L., Potts, G., Reddy, S., Spiess, R., Timms, N.E., Trimby, P., Wheeler, J., Zetterstrom, L., 1999. The application of electron backscatter diffraction and orientation contrast imaging in the SEM to textural problems in rocks. American Mineralogist 84, 1741–1759. https://doi.org/10.2138/am-1999-11-1204

Rowe, C.D., Griffith, W.A., 2015. Do faults preserve a record of seismic slip: A second opinion. Journal of Structural Geology 78, 1–26. https://doi.org/10.1016/j.jsg.2015.06.006

Rowe, C.D., Kirkpatrick, J.D., Brodsky, E.E., 2012. Fault rock injections record paleo-earthquakes. Earth and Planetary Science Letters 335–336, 154–166. https://doi.org/10.1016/j.epsl.2012.04.015

Shigematsu, N., Fujimoto, K., Ohtani, T., Goto, K., 2004. Ductile fracture of fine-grained plagioclase in the brittle–plastic transition regime: implication for earthquake source nucleation. Earth and Planetary Science Letters 222, 1007–1022. https://doi.org/10.1016/j.epsl.2004.04.001

Sibson, R.H., 1975. Generation of pseudotachylyte by ancient seismic faulting. Geophysical Journal International 43, 775–794.

Simpson, C., 1985. Deformation of granitic rocks across the brittle-ductile transition. Journal of Structural Geology 7, 503–511. https://doi.org/10.1016/0191-8141(85)90023-9

Stewart, C.A., Miranda, E.A., 2017. The Rheological Evolution of Brittle-Ductile Transition Rocks During the Earthquake Cycle: Evidence for a Ductile Precursor to Pseudotachylyte in an Extensional Fault System, South Mountains, Arizona. Journal of Geophysical Research: Solid Earth. https://doi.org/10.1002/2017JB014680

908 Swanson, M.T., 1988. Pseudotachylyte-bearing strike-slip duplex structures in the
909 Fort Foster Brittle Zone, S. Maine. Journal of Structural Geology 10, 813–
910 828. https://doi.org/10.1016/0191-8141(88)90097-1
911 Tchalenko, J.S., Ambraseys, N.N., 1970. Structural Analysis of the Dasht-e Bayaz
912 (Iran) Earthquake Fractures. Geological Society of America Bulletin 81, 41.
913 https://doi.org/10.1130/0016-7606(1970)81[41:SAOTDB]2.0.CO;2
914 Thielmann, M., Kaus, B.J.P., 2012. Shear heating induced lithospheric-scale
915 localization: Does it result in subduction? Earth and Planetary Science Letters
916 359–360, 1–13. https://doi.org/10.1016/j.epsl.2012.10.002
917 Viegas, G., Menegon, L., Archanjo, C., 2016. Brittle grain-size reduction of
918 feldspar, phase mixing and strain localization in granitoids at mid-crustal
919 conditions (Pernambuco shear zone, NE Brazil). Solid Earth 7, 375–396.
920 https://doi.org/10.5194/se-7-375-2016
921 Wehrens, P., Berger, A., Peters, M., Spillmann, T., Herwegh, M., 2016.
922 Deformation at the frictional-viscous transition: Evidence for cycles of fluid-
923 assisted embrittlement and ductile deformation in the granitoid crust.
924 Tectonophysics 693, 66–84. https://doi.org/10.1016/j.tecto.2016.10.022
925 Weinberg, R.F., Regenauer-Lieb, K., 2010. Ductile fractures and magma
926 migration from source. Geology 38, 363–366.
927 White, J.C., 2012. Paradoxical pseudotachylyte - Fault melt outside the
928 seismogenic zone. Journal of Structural Geology 38, 11–20.
929 https://doi.org/10.1016/j.jsg.2011.11.016
930 White, J.C., 2005. Transient Creep and Mechanical Instabilities in the Lower
931 Crust: the Long and the Short of It All. AGU Fall Meeting Abstracts.
932 White, J.C., 2004. Instability and localization of deformation in lower crust
933 granulites, Minas fault zone, Nova Scotia, Canada. Geological Society,
934 London, Special Publications 224, 25–37.
935 https://doi.org/10.1144/GSL.SP.2004.224.01.03
936 White, J.C., 2003. Windows of Transient Creep and Rupture in Continental
937 Lithosphere. AGU Fall Meeting Abstracts.
938 White, J.C., 1996. Transient discontinuities revisited: pseudotachylyte, plastic
939 instability and the influence of low pore fluid pressure on deformation
940 processes in the mid-crust. Journal of Structural Geology 18, 1471–1486.
941 https://doi.org/10.1016/S0191-8141(96)00059-4

White, S.H., Burrows, S.E., Carreras, J., 1980. On mylonites in ductile shear zones. Journal of Structural Geology 2, 175–187.

Wilde, S.A., Middleton, M.F., Evans, B.J., 1996. Terrane accretion in the southwestern Yilgarn Craton: evidence from a deep seismic crustal profile. Precambrian Research 78, 179–196.

Wyche, S., Ivanic, T., Zibra, I., 2013. Youanmi and Southern Carnarvon seismic and magnetotelluric (MT) workshop 2013. Geological Survey of Western Australia, Record 6, 180 p. Available at: http://dmpbookshop.eruditetechnologies.com.au/product/youanmi-and-southern-carnarvon-seismic-and-magnetotelluric-mt-workshop-2013.do

Wyche, S., Kirkland, C.L., Riganti, A., Pawley, M.J., Belousova, E., Wingate, M.T.D., 2012. Isotopic constraints on stratigraphy in the central and eastern Yilgarn Craton, Western Australia. Australian Journal of Earth 59, 657–670. https://doi.org/10.1080/08120099.2012.697677

Zibra, I., Clos, F., Weinberg, R.F., Peternell, M., 2017a. The ~2730 Ma onset of the Neoarchean Yilgarn Orogeny. Tectonics 36, 1787–1813. https://doi.org/10.1002/2017TC004562

Zibra, I., Gessner, K., Smithies, R.H., Peternell, M., 2014a. On shearing, magmatism and regional deformation in Neoarchean granite-greenstone systems: Insights from the Yilgarn Craton. Journal of Structural Geology 67, 253–267. https://doi.org/10.1016/j.jsg.2013.11.010

Zibra, I., Korhonen, F.J., Peternell, M., Weinberg, R.F., Romano, S.S., Braga, R., De Paoli, M.C., Roberts, M., 2017b. On thrusting, regional unconformities and exhumation of high-grade greenstones in Neoarchean orogens. The case of the Waroonga Shear Zone, Yilgarn Craton. Tectonophysics 712–713, 362–395. https://doi.org/10.1016/j.tecto.2017.05.017

Zibra, I., Smithies, R.H., Wingate, M.T.D., Kirkland, C.L., 2014b. Incremental pluton emplacement during inclined transpression. Tectonophysics 623, 100–122. https://doi.org/10.1016/j.tecto.2014.03.020

Figure captions

Fig. 1. Geological setting of the Cundimurra Shear Zone. (a) Simplified sketch of the Yilgarn Craton showing the subdivision into main terranes, and the location of the studied shear zone (Cundimurra Shear Zone, CMSZ). Terrane nomenclature after Cassidy et al. (2006). EGST: Eastern Goldfields Superterrane. (b) Geological sketch map of the Cundimurra Pluton/Shear Zone. Rectangle shows location of the study area and figure 2. "GR" indicates the Garden Rock Monzogranite. (c) Three-dimensional sketch summarizing the main geometric and kinematic features of the Cundimurra Pluton/Shear Zone, as constrained by field and geophysical data. Modified after Zibra et al. (2014b).

Fig. 2. Geological map of the Lake Austin Shear Zone, showing the spatial distribution of the main structural domains. Inset (a) shows an equal-area projection plot of the solid-state fabric (S_{MT} and L_{MT}) predating the Moyagee fault. For each equal-area projection, within brackets: number of measurements (n) and mean value (symbol). Inset (b) shows the orientation of the main fabric in the Golconda mylonite, postdating the Moyagee fault. Inset (c) shows the orientation of the gneissic foliation and mineral lineation (S_G and L_G, respectively) in host greenstones. Inset (d) shows the distribution of the magmatic foliation within the undeformed, c. 2620 Ma Garden Rock Monzogranite, which postdates all the shearing events in the study area.

Fig. 3. (a) Geological map of the Moyagee fault, showing geometric relations between the western pluton boundary, the steeply-dipping S_{MT} and the fault network. (b) Sketch illustrating an ideal fault array in a dextral, synthetic driven Riedel shear zone. Modified after Ahlgren (2001). (c) and (d) show the two equal-area stereographic projections for orientations of main structural elements. In (c), S_U and L_U refer to cataclasite-derived ultramylonites. In (d), S_{CAT} and L_{CAT} refer to foliation and lineation (the latter indicated by slickensides) in undeformed cataclasites, respectively. S_{OBL} and L_{OBL} refer to fault segments at high angle from the main fault surfaces. Symbols near the number of measurements indicate mean values.

1005 **Fig. 4**. Detailed maps of the Moyagee fault, obtained by a combination of
1006 orthophoto observations and conventional structural mapping. Fig. 4. (a)
1007 The Moyagee fault is an array of left-stepping en-echelon fault segments
1008 with R-type orientation (red) relative to the western boundary of the
1009 Cundimurra Pluton. Shorter faults with P-type orientation (red) link the en
1010 echelon segments. (b) Detailed fault map shows the fault network
1011 configuration to be consistent across several orders of magnitude. (c) Map
1012 of a complex brittle fault segment comprised of parallel fault traces with cm-
1013 scaling spacing and minimal ductile overprint. The fault segment terminates
1014 southward in an array of small, horse-tailing reverse faults. (d) Histograms
1015 of orientation data of veins for the Moyagee fault, including all data from
1016 undeformed cataclasites and cataclasite-derived ultramylonites.

1017 **Fig. 5**. (a) Horizontal pavement as an image and interpreted drawing showing a
1018 representative example of paired fault surfaces, developed along the
1019 contact between a gneissic pegmatite and host granitic gneiss. Insets of
1020 equal-area plots show orientation of the mylonitic foliation and lineation at
1021 each locality. Inset at lower right sketches the main types of Riedel shears
1022 observed in this outcrop. Main Y-shears are ~50 cm apart, connected by
1023 synthetic R-shears. Along the lithological boundary, granitic gneiss
1024 contains a dense network of shear surfaces sub-parallel to the main Y-
1025 shear. Figures (b) – (f) show detailed outcrop-scale images and maps of
1026 three portions of the fault network shown in Figure 4c, which is devoid of
1027 any ductile overprint. (b) The domain comprised between the paired faults
1028 developed a dense network of fractures, associated with large volumes of
1029 tourmaline-rich veins. Main Y-shears are associated with high-angle T-
1030 fractures and are joined by synthetic R-shears. In foliated domains, the
1031 overall sigmoidal shape of clasts, or clast aggregates, is in agreement with
1032 the dominant dextral shear sense. (c) Close-up view of the planar, central
1033 part of (b) showing an array of nearly evenly-spaced, tourmaline-filled veins
1034 at high-angle to the fault surface. (d) Detail of well-developed antithetic R'-
1035 shears. Y-, R- and R'-shears, all nearly subvertical. (e) Complex fracture
1036 network developed within closely spaced, paired fault surfaces, some 10 m
1037 north from the fault network shown in (b). (f) The northernmost exposed

segment of this fault network shows two main paired surfaces, ~1.5 m apart, joined by partially developed synthetic R-shears. While the overall fracture geometry in this segment is similar to the one shown in (b), in this case the volume of tourmaline-rich veins is notably smaller. (g) Close-up view of a ~20 cm-thick mylonite zone developed along the lithological contact between a composite aplite-pegmatite vein and host granitic gneiss, from a 2 km-long, tourmaline-free fault segment, located at the southern end of the Moyagee fault (Fig. 3a). Note that pinch-and-swell structure occurs in the pegmatite layer only. Within the mylonite, S–C and C' subfabrics, together with sigmoidal feldspar porphyroclasts, indicate dextral shear sense. Protomylonitic granite flanking the northeastern side of the shear zone preserves a network of fractures and small-scale faults, suggesting that the mylonite developed at the expenses of a pre-existing cataclasite. Inset of equal-area plot shows orientation of the mylonitic foliation and lineation at this locality. (h) Representative example of "pseudotachylyte-like" fault surface, developed within an aplite vein. The vein is ~2 cm-thick, it contains a small proportion of clasts from host gneiss, and it is associated with cm-thick lateral veins resembling injection veins in pseudotachylytes. The trace of S_{MT} is highlighted by aligned mica flakes.

Fig. 6. (a) Horizontal exposure of a paired cataclasite-ultramylonite. The eastern side of this composite structure largely preserves outcrop-scale features recorded during cataclasite development, including randomly-oriented clast from host gneiss and high-angle, undeformed T-fractures with sub-millimetric thickness (arrowheads). In contrast, the western side of the vein contains a layered ultramylonite, derived from ductile deformation of cataclasite. Note the abrupt transition between weakly-deformed cataclasite and ultramylonite, marked by the yellow dashed line. Inset of equal-area plot shows orientation of the mylonitic foliation and lineation at this locality. (b) Polished hand sample (212727) from a paired cataclasite-ultramylonite. The ultramylonite developed at the expenses of cm-thick cataclasite, which is locally preserved along strike. Veins developed near the main rupture surface and pre-existing S_{MT} in the host were ductilely

deformed and rotated into parallelism with the ultramylonite. On the eastern side of the main surface, high-angle T surfaces are virtually undeformed, except for the region marked by (*), where mm-long segments of T veins were dextrally dragged into the ultramylonite. Microstructures from this sample are described in section 4.

Fig. 7. The role of lithological contacts in strain localization. Fig. 3 for photograph location. (a) Layered granitic gneiss at margins of the Moyagee fault, with aplites and pegmatites subparallel to S_{MT}. (b) Tourmaline-bearing cataclasite developed along the contact between an aplite vein and host granitic gneiss. White arrowhead points to a T-fracture whose orientation indicates dextral shear sense. Black arrowhead points to an isoclinally folded T-fracture, in the mylonitized portion of the aplite vein. Scale bar at lower right, in both (a) and (b), is 5 cm-long (c) Tourmaline-bearing ultramylonite developed along the contact between a gneissic pegmatite and host granitic gneiss. Internal layering in ultramylonite is likely due to sheared cataclasite clasts (compare with Fig. 6, from the same fault segment). Pencil for scale. (d) Tourmaline-bearing, layered ultramylonites developed along both lithological contacts between a gneissic pegmatite and host granitic gneiss. Along the lower contact, C shear bands in pegmatite indicate dextral shear sense, which is highlighted with a line drawing. (e) Shearband boudins developed in a sheared pegmatite near the margins of the Moyagee fault. Boudinage occurred along knife-sharp, synthetic shears that only developed near the pegmatite. Pen for scale. (f) Detail from a sigmoid-shaped boudin block bounded by shear bands. (g) Shear zone localized in aplite vein, showing ~1m of dextral displacement and subhorizontal stretching lineation (L_U), with line drawing in lower left to illustrate features and show the position of Figure 7h. Scale bar at lower right is 2 cm-long (h) Detail from (g) showing the knife-sharp transition between the sheared aplite and S_{MT} in host gneiss.

Fig. 8. (a) Geological map of the Pinnacles Domain, i.e. the northernmost segment of the Lake Austin Shear Zone. Inset of equal-area projection plot shows lineations and poles to foliation for both granitic gneiss and

greenstones. (b) Detail from a boudinaged granitic dyke, previously intruded into ultramafic schists ((a) shows location). Tourmaline-injected cataclasite developed along the contact between the granitic dyke and the quartz vein with both lithologies occurring as angular clasts in the cataclasite. (c) Detail from the same boudinaged granitic dyke shown in (b), here preserving a more a more advanced stage of brecciation with angular clasts deriving from the granite dyke and the adjacent, late-magmatic quartz vein. (d) Representative microstructure of tourmaline-rich veins associated with cataclasite in a boudinaged, mylonitic granite dyke. The vein recorded domino-type boudinage whose asymmetry indicating dextral shear sense, consistently with sigmoidal K-feldspar porphyroclasts (arrowhead). The granitic dyke shows a mylonitic foliation that predates boudinage and predates the emplacement of the tourmaline vein itself. Cross-polarized light.

Fig. 9. Main mesoscale features in the Golconda mylonite. (a) Horizontal exposure showing the prominent S-C fabric that typifies the Golconda mylonite. (b) Oblique view on a horizontal exposure showing mylonitic folds, with axial plane and fold axes sub-parallel to S_U and L_U, respectively. S_U is folded, indicating that these folds developed late in the shearing history. Closely-spaced ultramylonites likely nucleated on paired cataclasites (i.e. compare with figs 5a–f). (c) Horizontal (i.e. near XZ) exposure of a layered ultramylonite, developed at the expense of a former cataclasite. In the central, blue and white portion, compositional layering is likely defined by stretched clasts from host gneiss (i.e. compare with Fig. 6). In the gneissic portion of the shear zone, S-C fabric and C' shear bands indicate dextral shear sense. The layering is offset by a network of antithetic slip surfaces defining domino-type boudinage. Note that, in the upper part of the layer (in the domains indicated by "*"), mylonitic foliation is not deflected around offset boudin blocks, indicating that brittle deformation occurred at a very late stage of shearing. (d) Plurimetric, knife-sharp fault developed ~10° clockwise from the prominent C fabric, whose trace is indicated by the yellow dashed line. (e) Detail from (d) showing en

1135 echelon fault segments joined by high-angle wing cracks. Linkage occurs
1136 at right-stepping extensional stepovers (f) Sketch showing a model of fault
1137 development as conjugate R- shears and wing cracks (W), in relation to
1138 main slip surfaces, corresponding to the C fabric.

1139 **Fig. 10**. Subfigures (a)–(d): representative pre-cataclasite meso- and
1140 microstructures from granitic gneiss at margins of the Moyagee fault. All
1141 photomicrographs are cross-polarized, unless specified. (a) Polished hand
1142 sample from the contact between boudinaged pegmatite and host granitic
1143 gneiss (compare with Fig. 7f). Note that, in granitic gneiss, most
1144 plagioclase and K-feldspar porphyroclasts show evidence of cataclasis
1145 (one example is indicated by the red arrowhead). (b) high-strain version of
1146 S_{MT}, showing widespread brittle deformation in feldspar and lensoid quartz
1147 ribbons (the latter marked by white arrowheads). Antithetic microfaults in K-
1148 feldspar (yellow arrowhead) and small-scale shear bands (red arrowhead)
1149 indicate dextral shear sense. (c) Close-up view at a strain shadow domain
1150 (outlined by the yellow dashed lines) near a K-feldspar porphyroclast
1151 ("Kfs"). The strain shadow contains elongate aggregates of porphyroclast
1152 fragments, embedded within fine-grained recrystallized feldspar (10–20 μm
1153 in size). (d) Shear band sharply truncating S_{MT}, along the boundary
1154 between the boudinaged pegmatite and host granitic gneiss. Angular
1155 feldspar fragments preserved at the base of the photo are mantled by fine-
1156 grained recrystallized feldspar, in analogy with what shown in (c).
1157 Subfigures (e) to (h): sample 212762, representative of an undeformed
1158 cataclasite. (e) Hand sample of a "pseudotachylyte-like" injection vein, at
1159 high-angle to S_{MT} in host gneiss. (f) Micrograph from the central portion of
1160 the vein shown in (e), here at moderate angle from S_{MT} in host gneiss. The
1161 vein contains mm-sized tourmaline$_1$ grains, now replaced by finer-grained
1162 tourmaline$_2$, and angular to rounded clasts from the host gneiss. Note the
1163 elongate trails of fine-grained recrystallized feldspar in host gneiss
1164 (indicated by the red dashed line), defining the ultramylonite domain
1165 ("Umyl"). Mineral abbreviations after Kretz (1983). All thin sections were
1166 prepared along the XZ sections of the finite strain ellippsoid; that is,
1167 perpendicular to S_{MT} and parallel to L_{MT} in the cataclasite, and

perpendicular to S_U and parallel to L_U for the ultramylonite. (g) Ultramylonite layer, marked by completely recrystallized feldspar (10–20 μm in size), along the contact between cataclasite and host gneiss. Note that quartz lenses contain polygonal, apparently strain-free grains. Ultramylonite is cut by ~50 μm-thick cataclasite veins (arrowhead), branching off the main fault surface. (h) Close-up view from (g), showing portions of ultramylonite as fragments within the tourmaline-bearing cataclasite.

Fig. 11. Representative microstructures from mylonites and ultramylonites. (a) Whole-thin section micrograph showing the relationships between P and T surfaces and the ultramylonite. Compare with Fig. 7. Rectangles show location of additional micrographs from the same sample. Plane polarized light. (b) SEM-BSE image of a transposed and mylonitized vein. Note the shape preferred orientation and the pinch and swell of lensoid quartz ribbon. (c) Mylonite domain, in a zone of transposed T_1 veins, which are mainly composed by ultrafine (~1–10μm) $tourmaline_2$ aggregates. Shear band type feldspar porphyroclasts (near the centre) prevail in this domain. (d) SEM-BSE image of the ultramylonite microstructure. The image shows the contact between the granitic ultramylonite on the left side and the ultramylonite derived from the tourmaline-rich cataclasite on the right side. (e) EDS-derived compositional maps of part of the ultramylonite microstructure shown in (d). Note the thin films of K-feldspar filling the incipient gaps between quartz grains in a polycrystalline quartz ribbon. Domino-type boudinage in quartz ribbon indicates dextral shear sense. Note that these maps show the same boudinaged quartz ribbon shown in the left part of (d). However, the actual frame of (e) is not included in (d). (f) Pinch-and-swell and boudinage in a one-grain-thick quartz ribbons (central layer). Boudin neck infill is matrix feldspar (e.g. see the yellow, wedge-shaped K-feldspar grain near the centre). Gypsum plate inserted. (g) SEM-BSE image of the ultrafine-grained matrix of the tourmaline-rich ultramylonite. At left, a boudinaged quartz ribbon shows K-feldspar infill. (h) Close-up view on compositional layering in the ultramylonite domain. Dark layers are 10–20 μm-thick and contain euhedral, aligned $tourmaline_2$

grains. Other tourmaline$_2$ grains are dispersed in the quartzofeldspathic polygonal aggregate (white), where average grain size is ~10–20 μm. Plane polarized light. (i) Festoons of isolated polycrystalline quartz lenses and opaque aggregates defining C′-type bands in the quartzofeldspathic ultramylonite matrix.

Fig 12. Quartz CPO data from the ultramylonite, obtained by using an automated fabric analyser microscope (sample 198170) and with EBSD analysis (sample 212727). (a) Pole figures of quartz grains in polycrystalline ribbons. For sample 212727, the following crystallographic directions and poles to planes were plotted: c-axis <0001>, a-axis {11-20}, prism plane {10-10}, positive rhombohedral plane {10-11}, negative rhombohedral plane {01-11}. Data are plotted as one point per grain (N = number of grains). In both samples, the quartz c-axis fabric opening angle, measured across the Z axis, is about 70–75°. (b) Inverse Pole Figure (IPF) map of tourmaline, colour-coded with respect to the stretching lineation of the ultramylonite. The inset shows the IPF of tourmaline. Grain boundaries (misorientation > 10°) are shown in black, low-angle boundaries (misorientation between 2° and 10°) are shown in cyan. Grey areas represent unindexed points. (c) Pole figures of the tourmaline grains from the map shown in (b). Plotted crystallographic directions and poles to planes are: c-axis <0001>, prism plane {10-10}. Data are plotted as one point per grain (N = number of grains). In both (a) and (c), maxima are expressed as multiples of the uniform distribution.

Fig 13. (a) Sketch illustrating the inferred transition from dominantly ductile high-strain zones developed along lithological contacts to cataclasite. Redrawn after Figs. 5b, 7b, e and f. (b) Idealized sketch showing the early stages of development of the Lake Austin Shear Zone, with development of the two main networks of brittle structures (the Moyagee and Pinnacles faults), in turn overprinted by localized ultramylonites. (c) Further shearing along the Lake Austin Shear Zone was accommodated by shear zone broadening

1233 with the development of the Golconda mylonite, overprinting brittle and
1234 ductile structures. (d) Equal-area projection plots for each deformation
1235 stage. Note that the kinematic framework developed during the late stages
1236 of pluton emplacement (represented by S_{MT} and L_{MT}) remains unchanged
1237 during the development of the Lake Austin Shear Zone. Symbols near the
1238 number of measurements indicate mean values.

1239

1240

1241

1242

1243

1244

1245

1246

1247

1248

1249

1250

1251

1252

1253

1254

1255

*Figure 1
Click here to download high resolution image

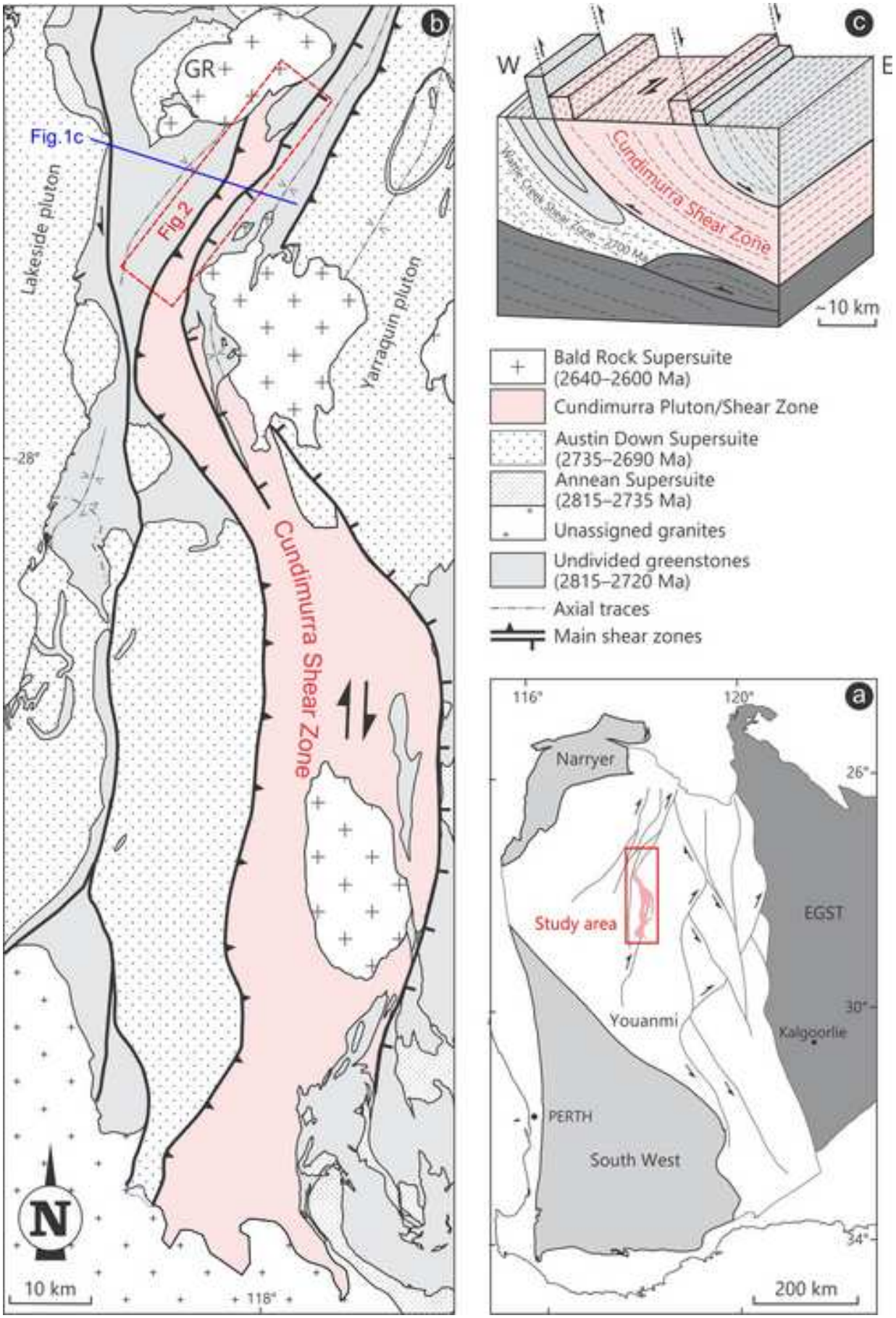

*Figure 2
Click here to download high resolution image

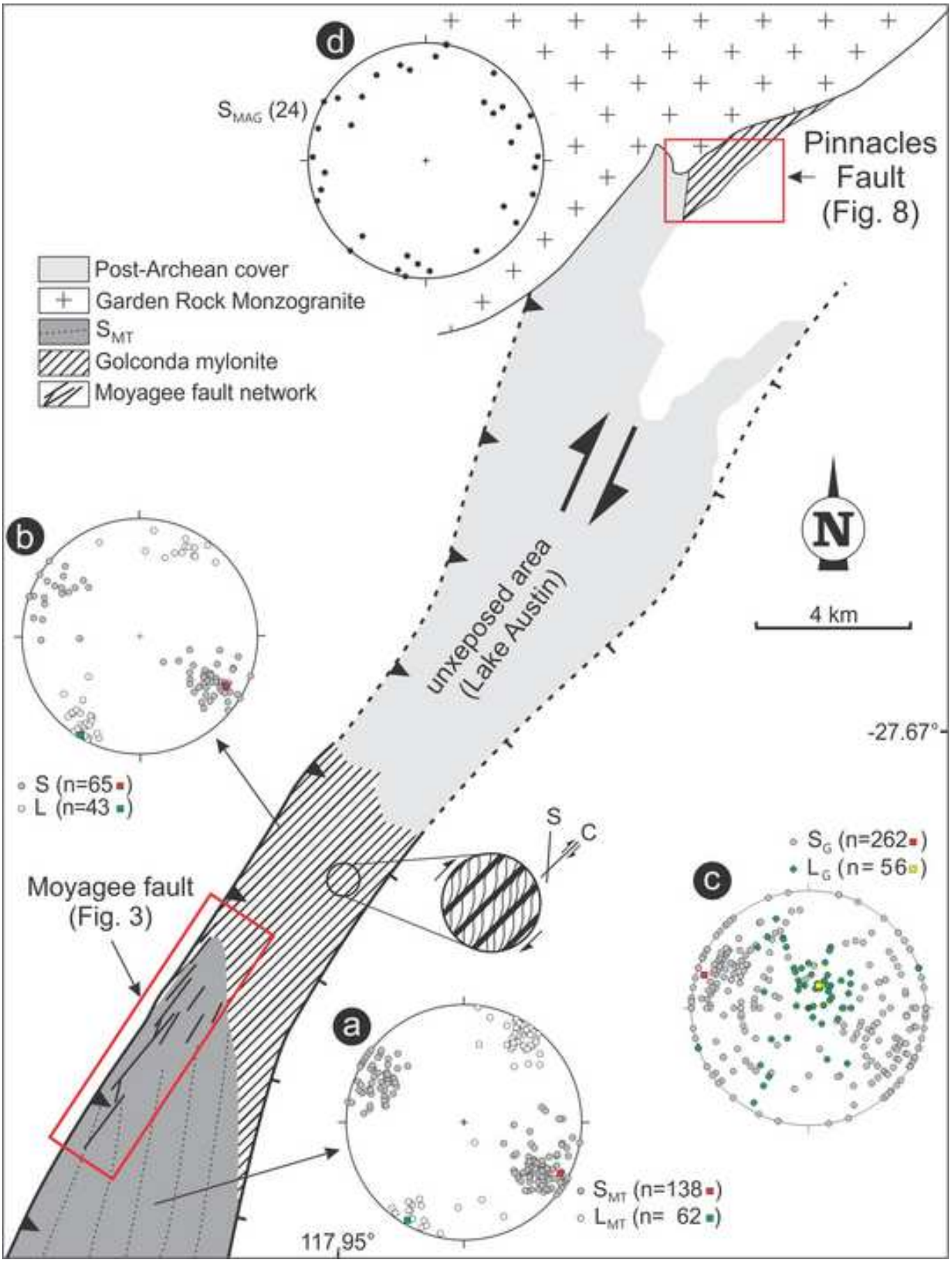

*Figure 3
Click here to download high resolution image

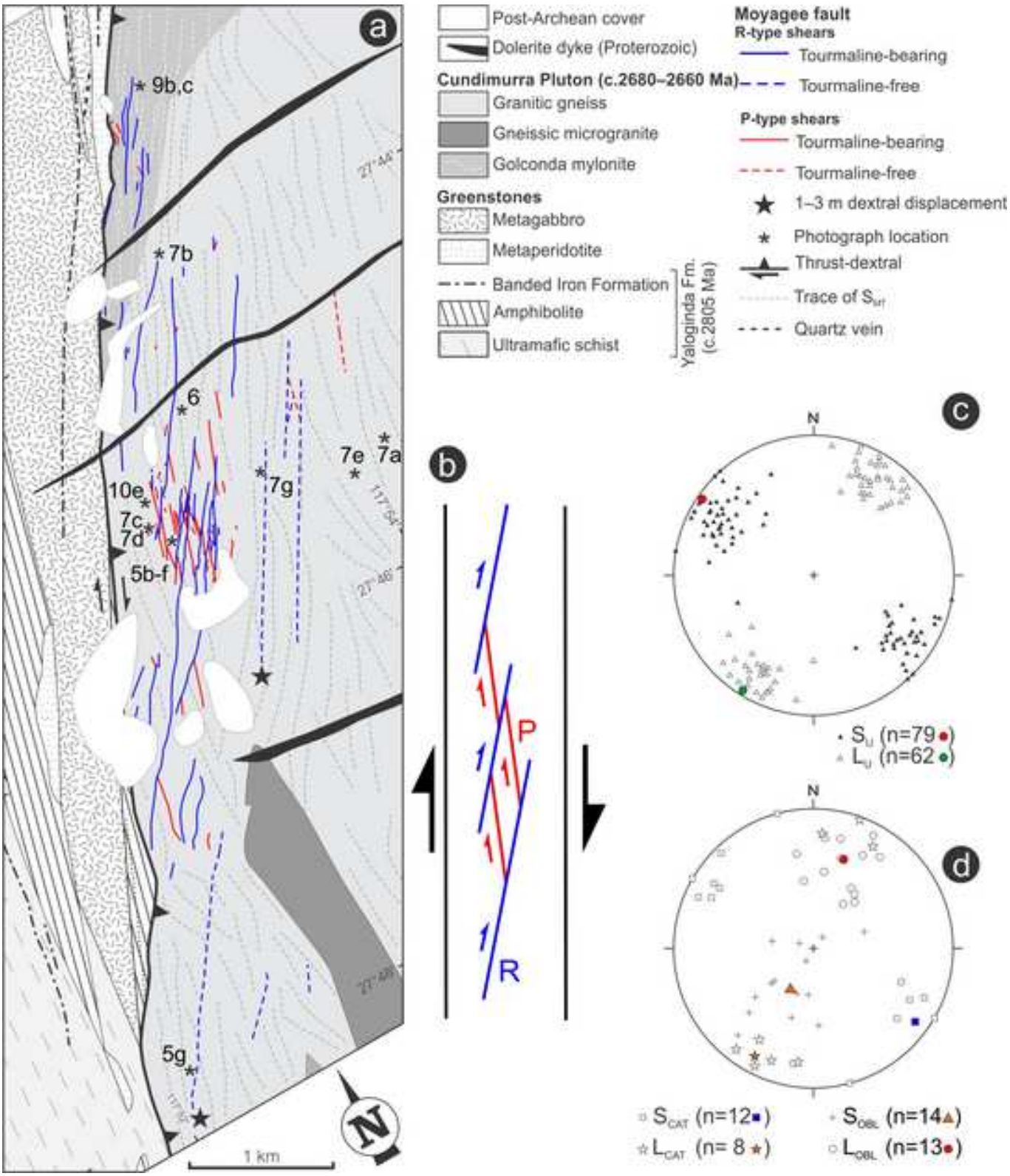

*Figure 4ac
Click here to download high resolution image

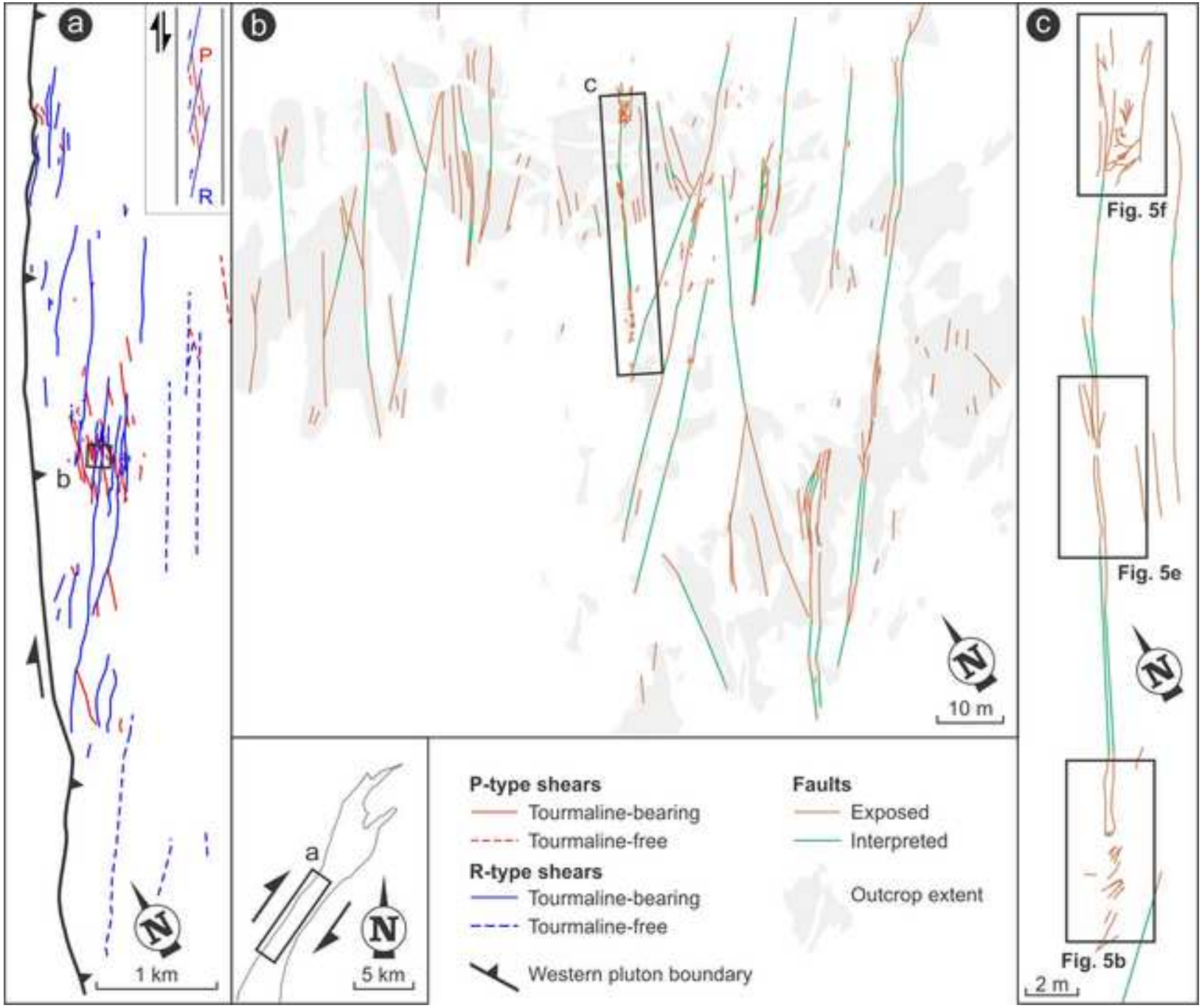

*Figure 4d
Click here to download high resolution image

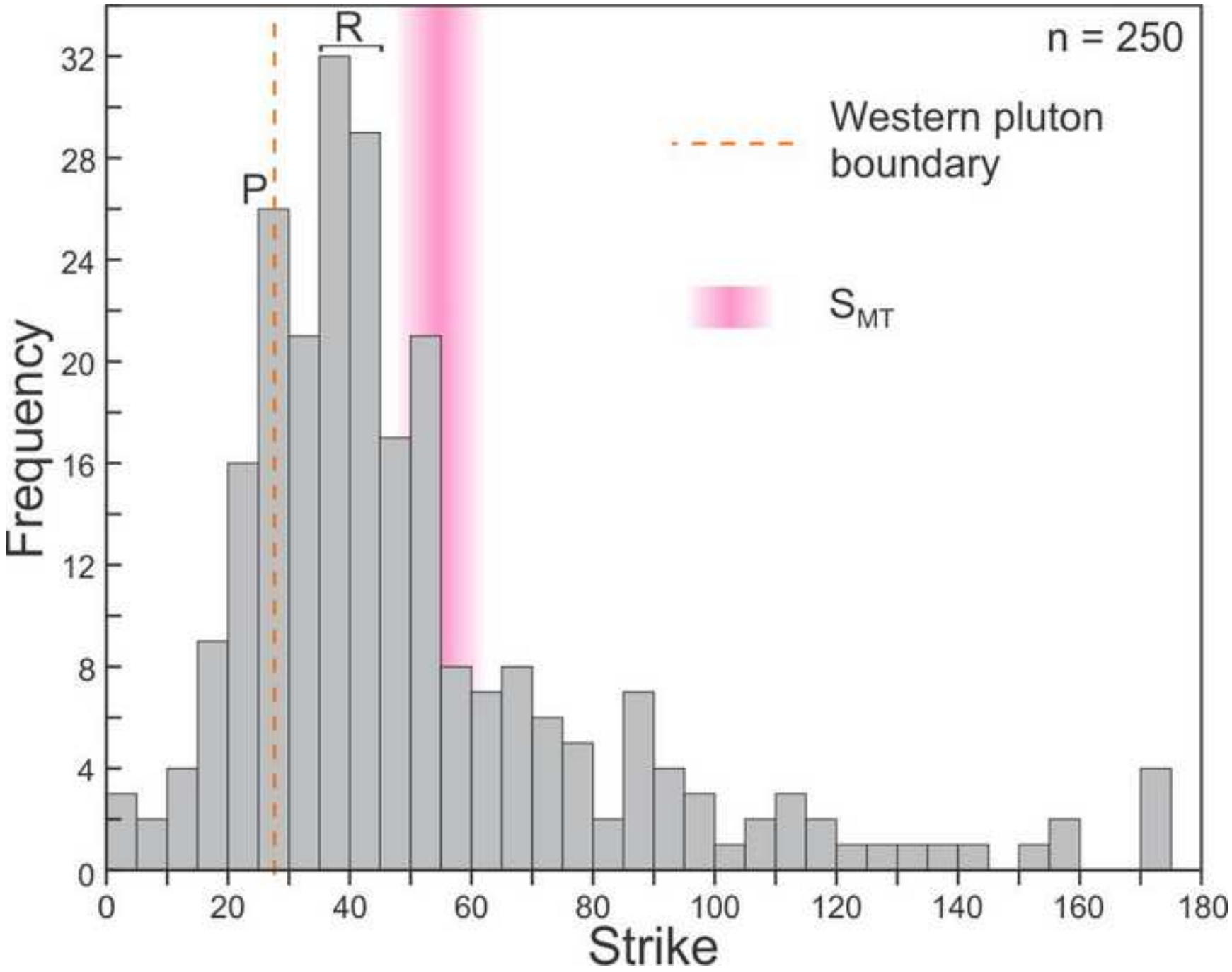

*Figure 5a
Click here to download high resolution image

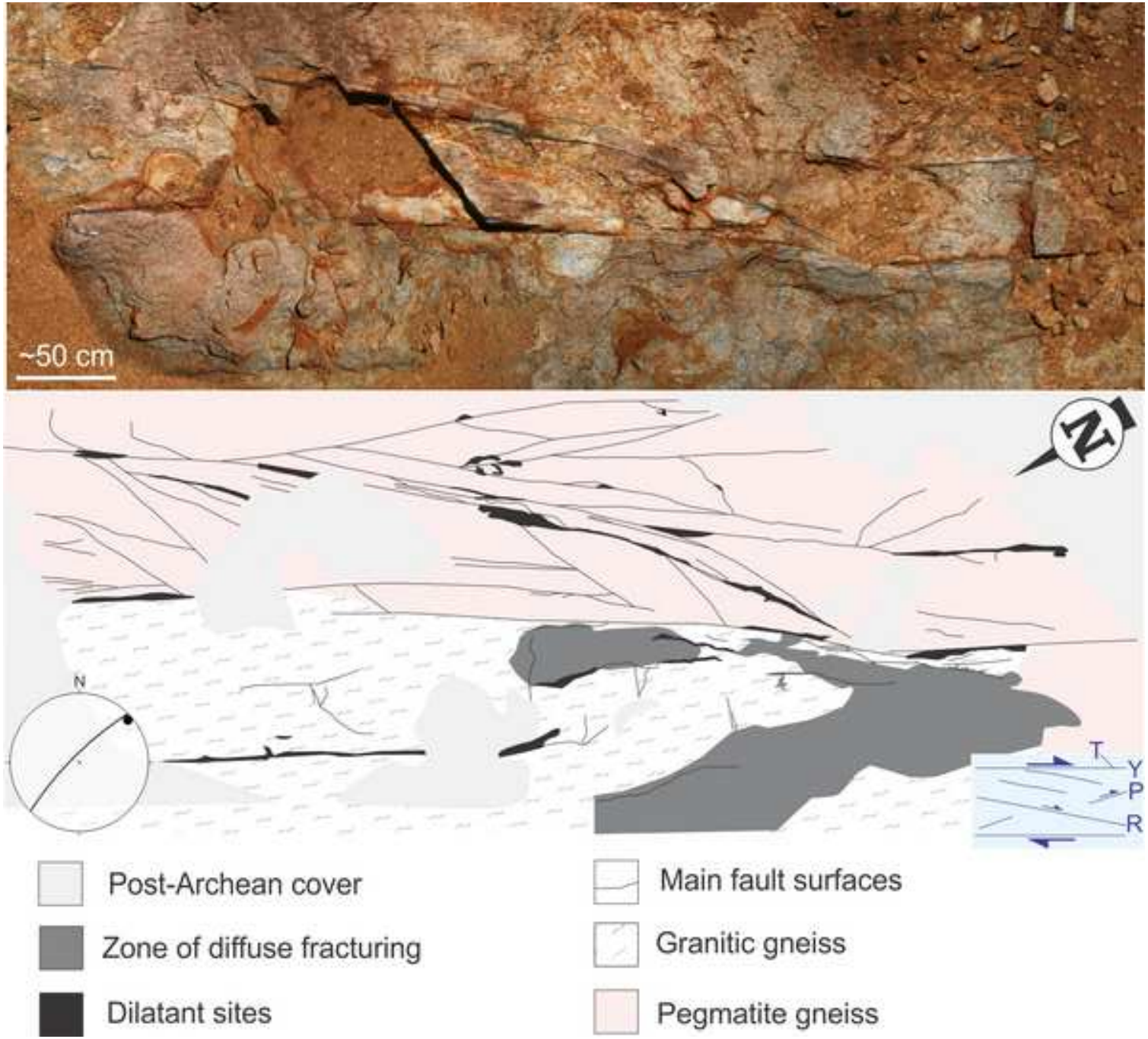

*Figure 5bd
Click here to download high resolution image

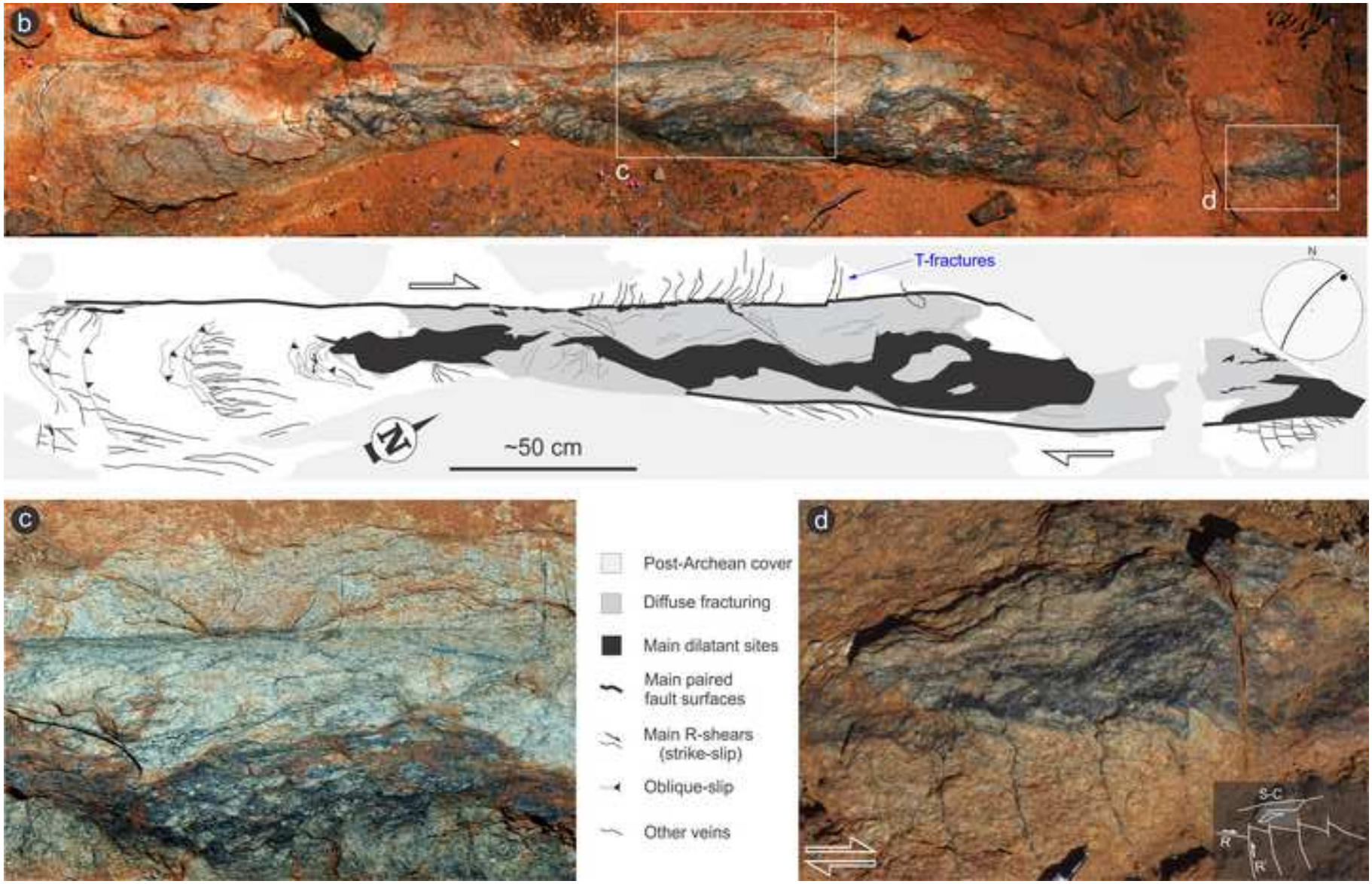

***Figure 5ef**

Click here to download high resolution image

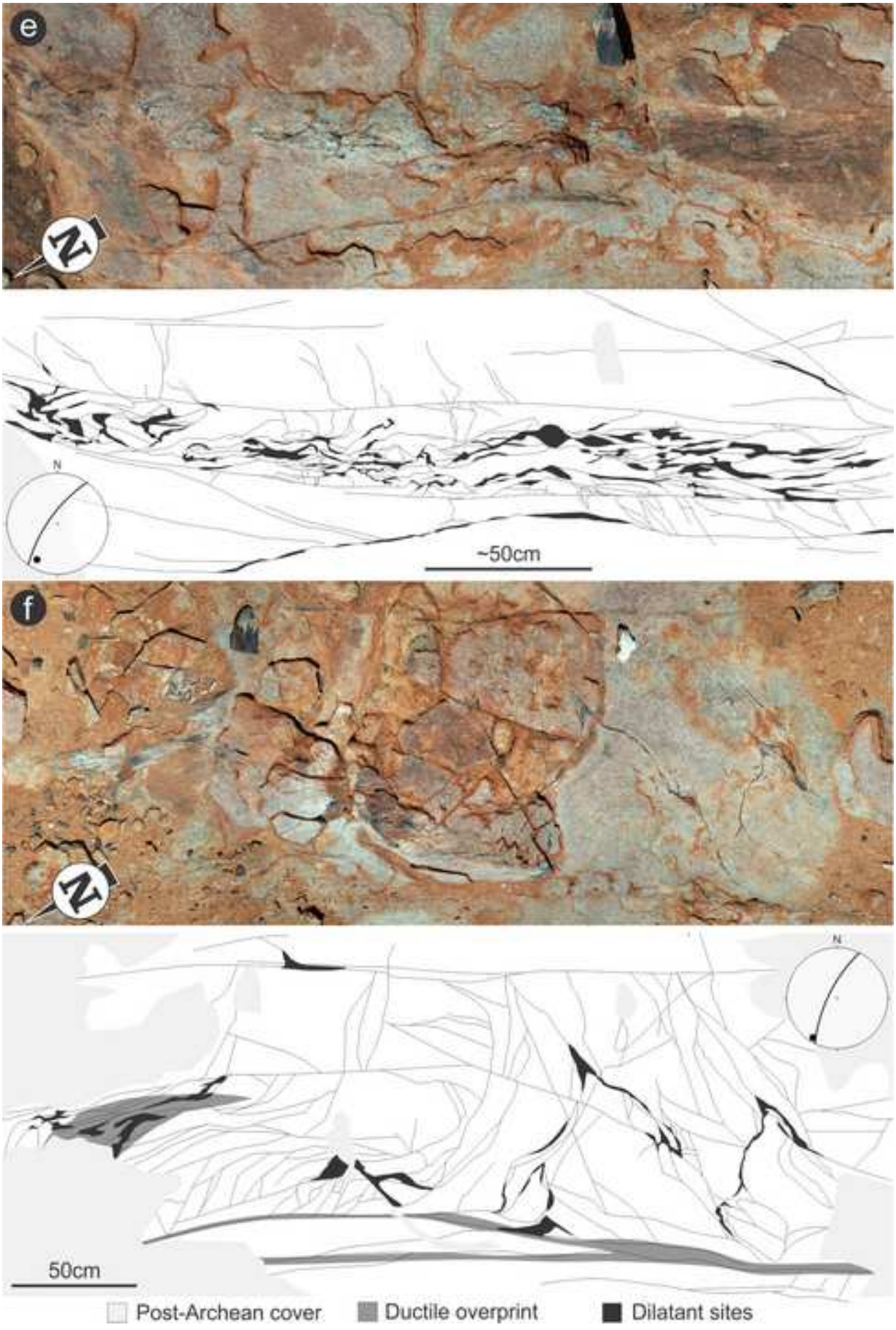

*Figure 5h
Click here to download high resolution image

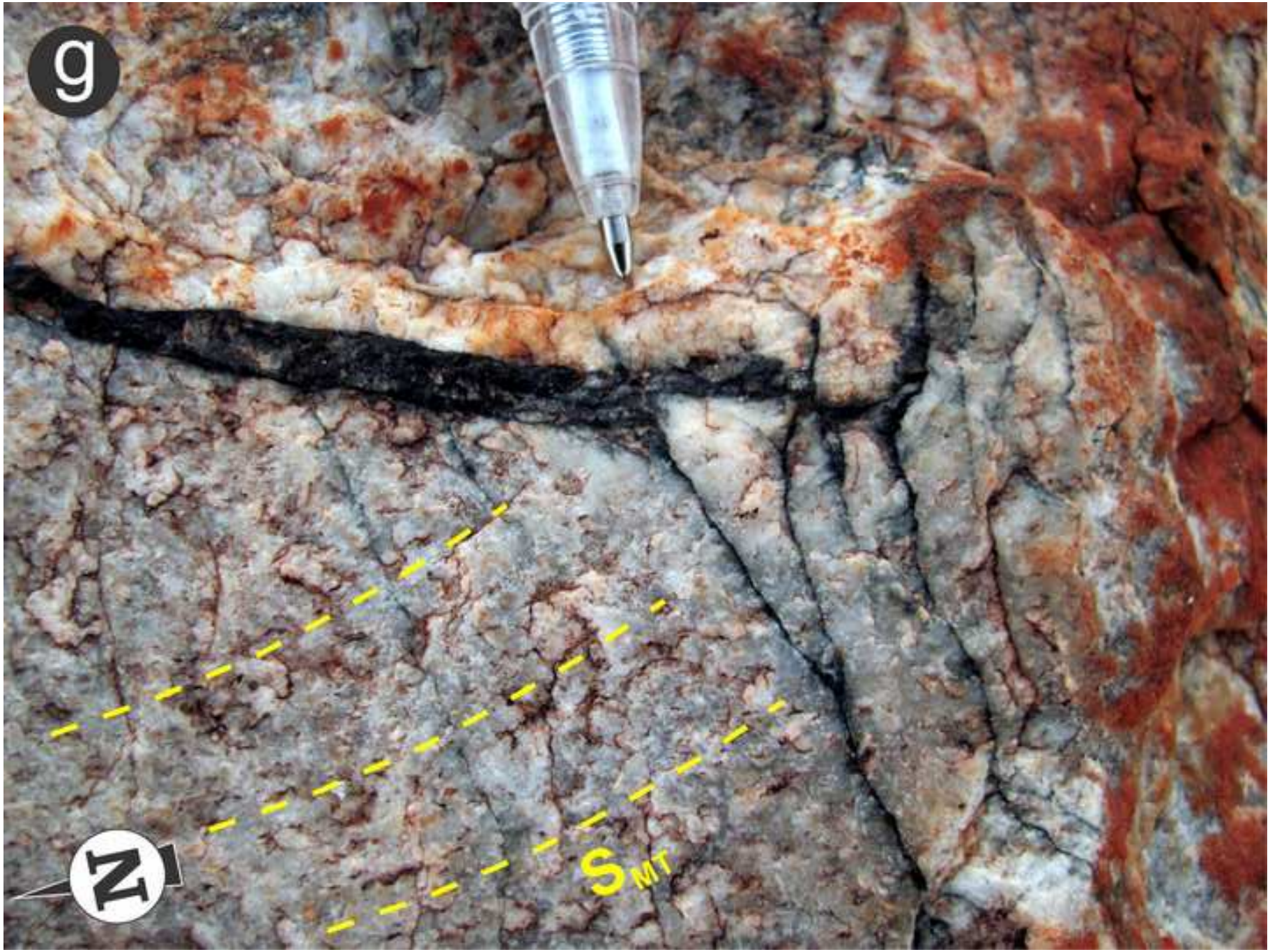

*Figure 5g
Click here to download high resolution image

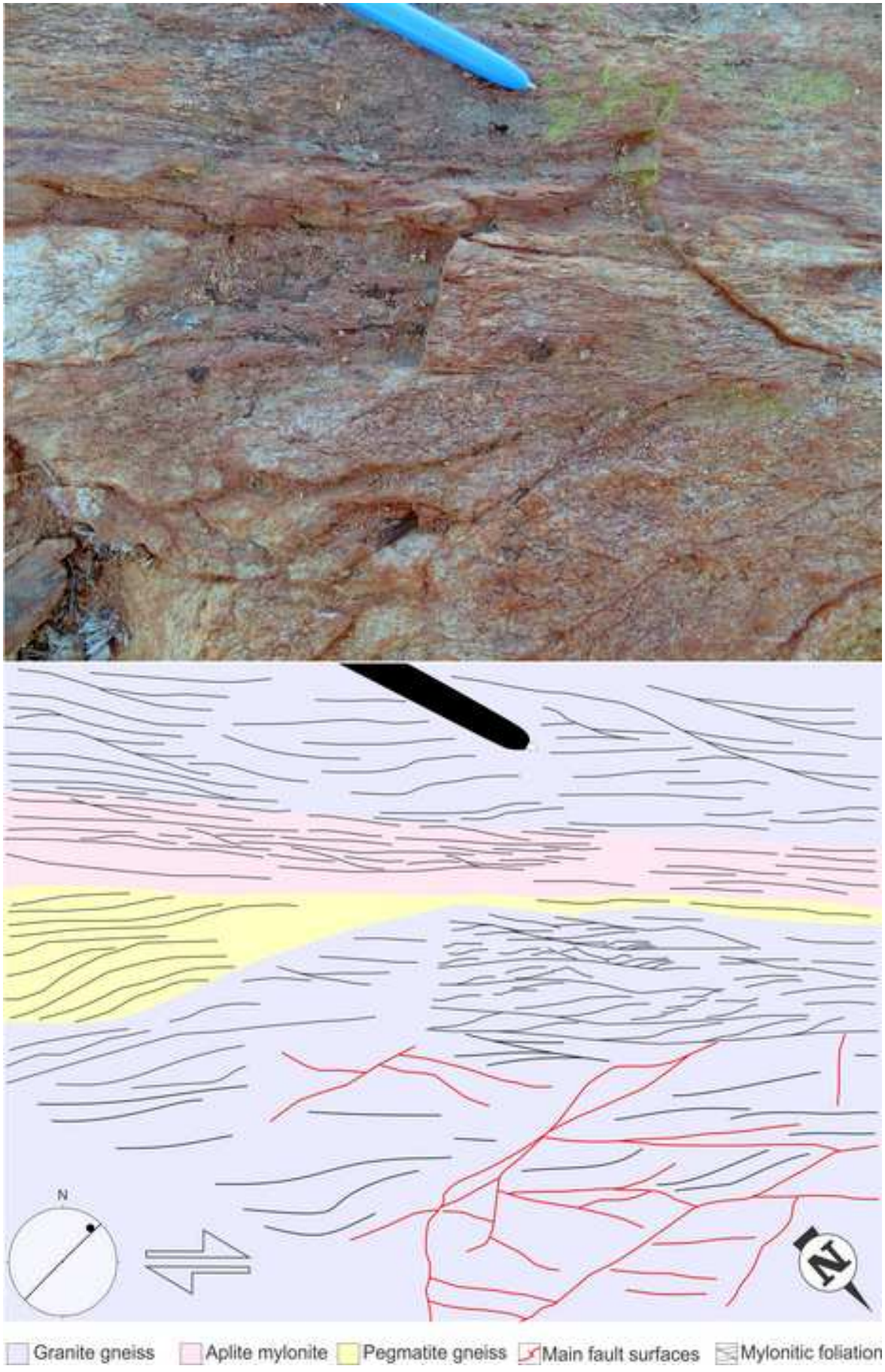

***Figure 6ab**

Click here to download high resolution image

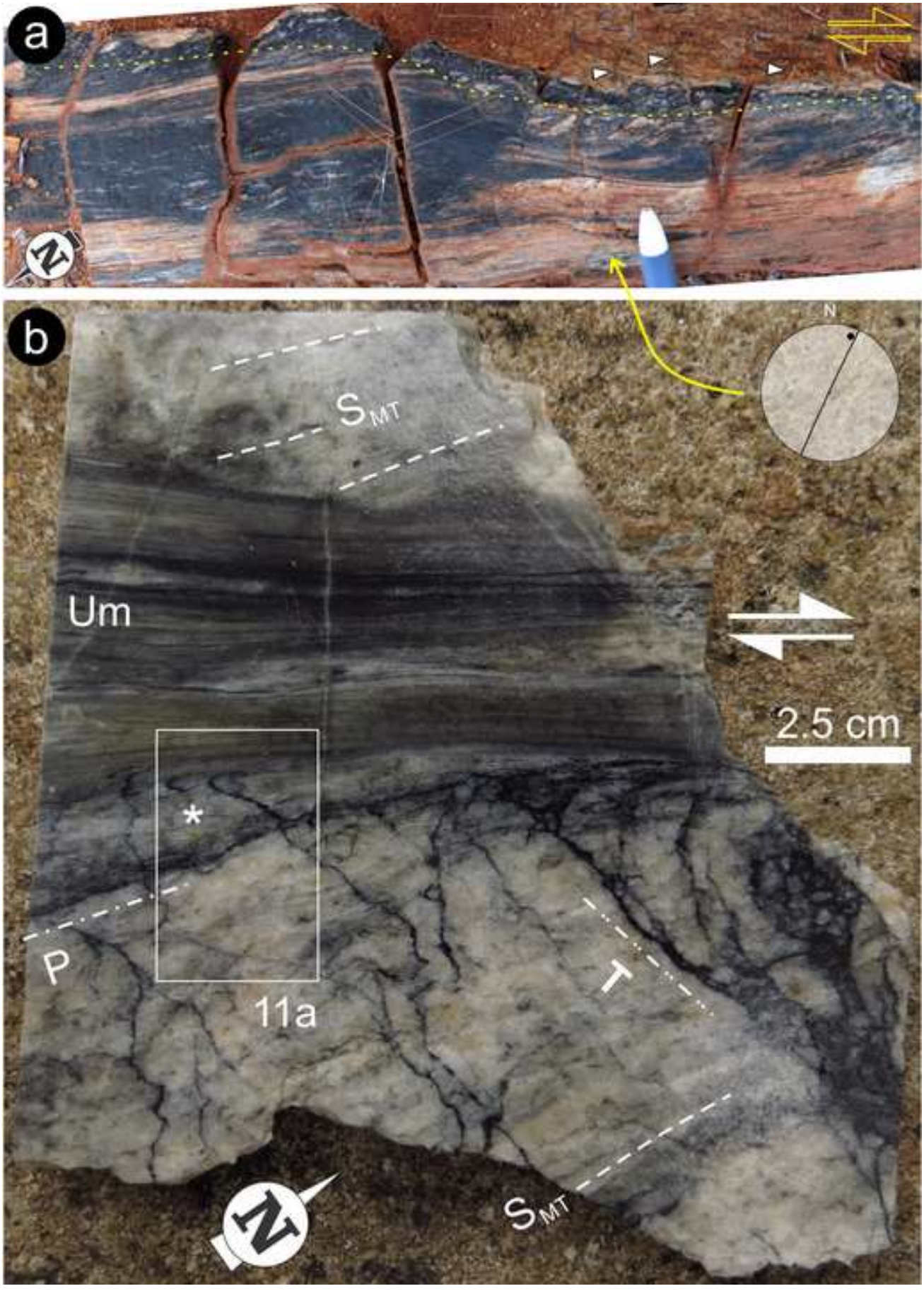

*Figure 7
Click here to download high resolution image

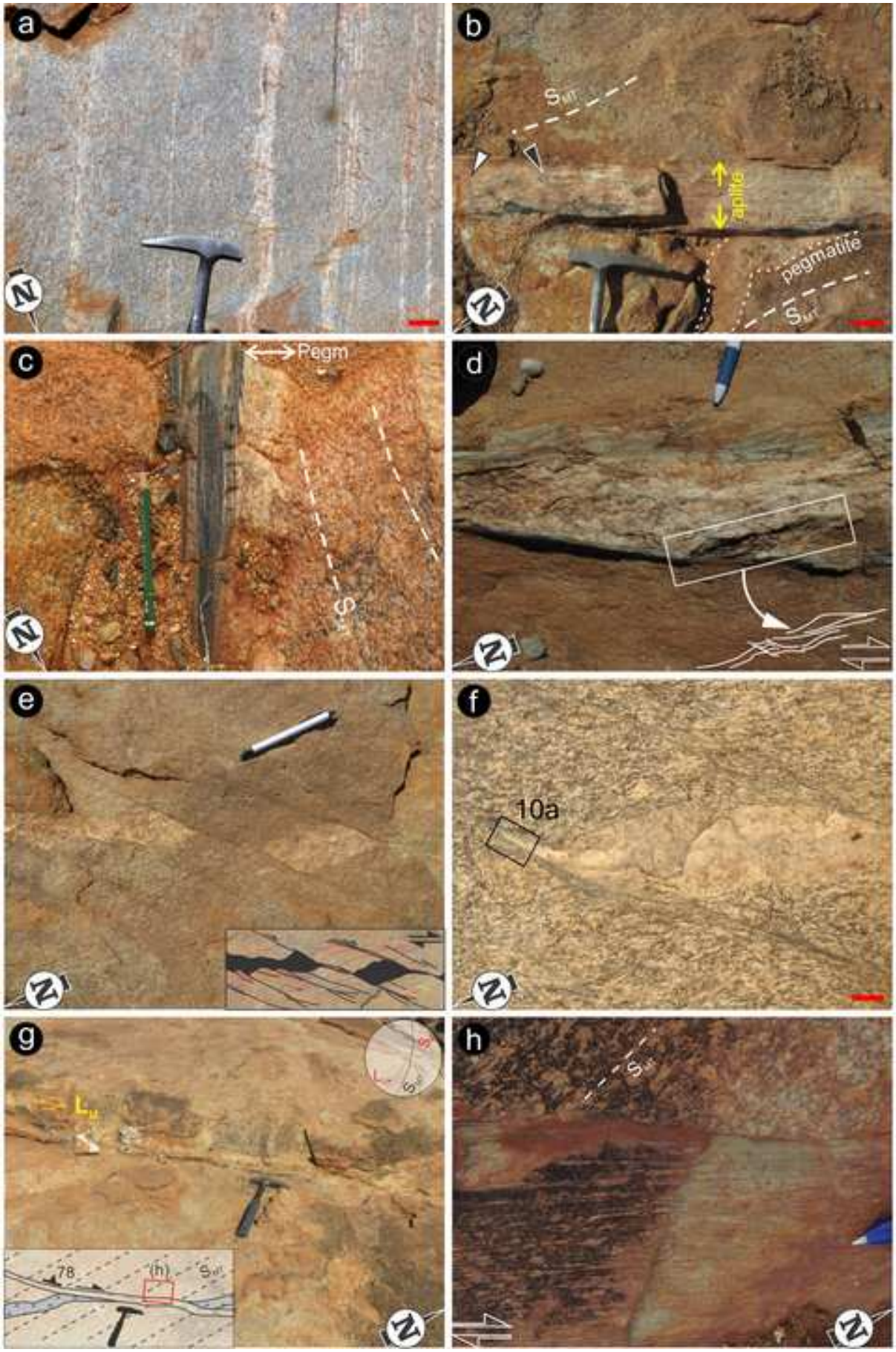

*Figure 8
Click here to download high resolution image

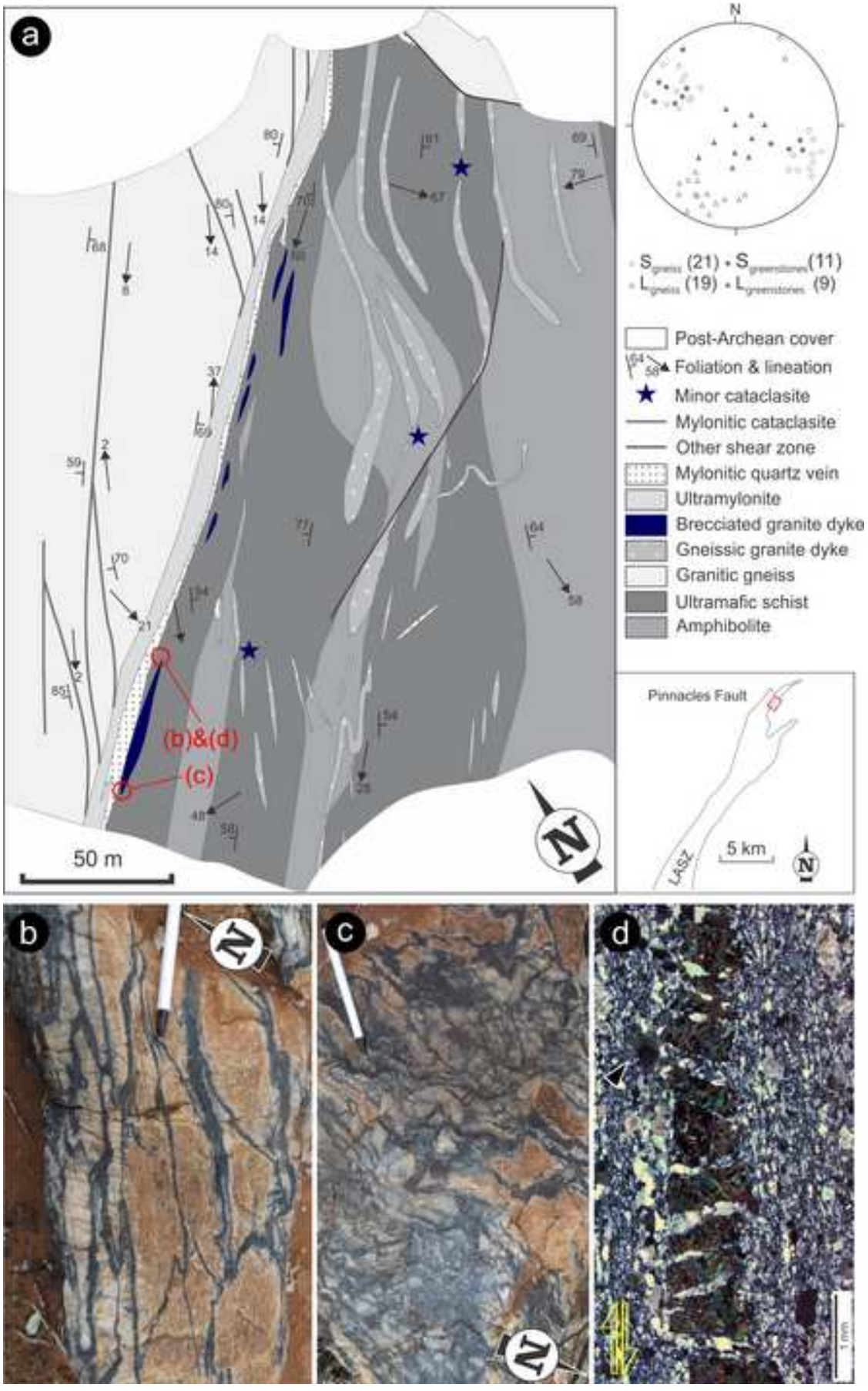

*Figure 9ac
Click here to download high resolution image

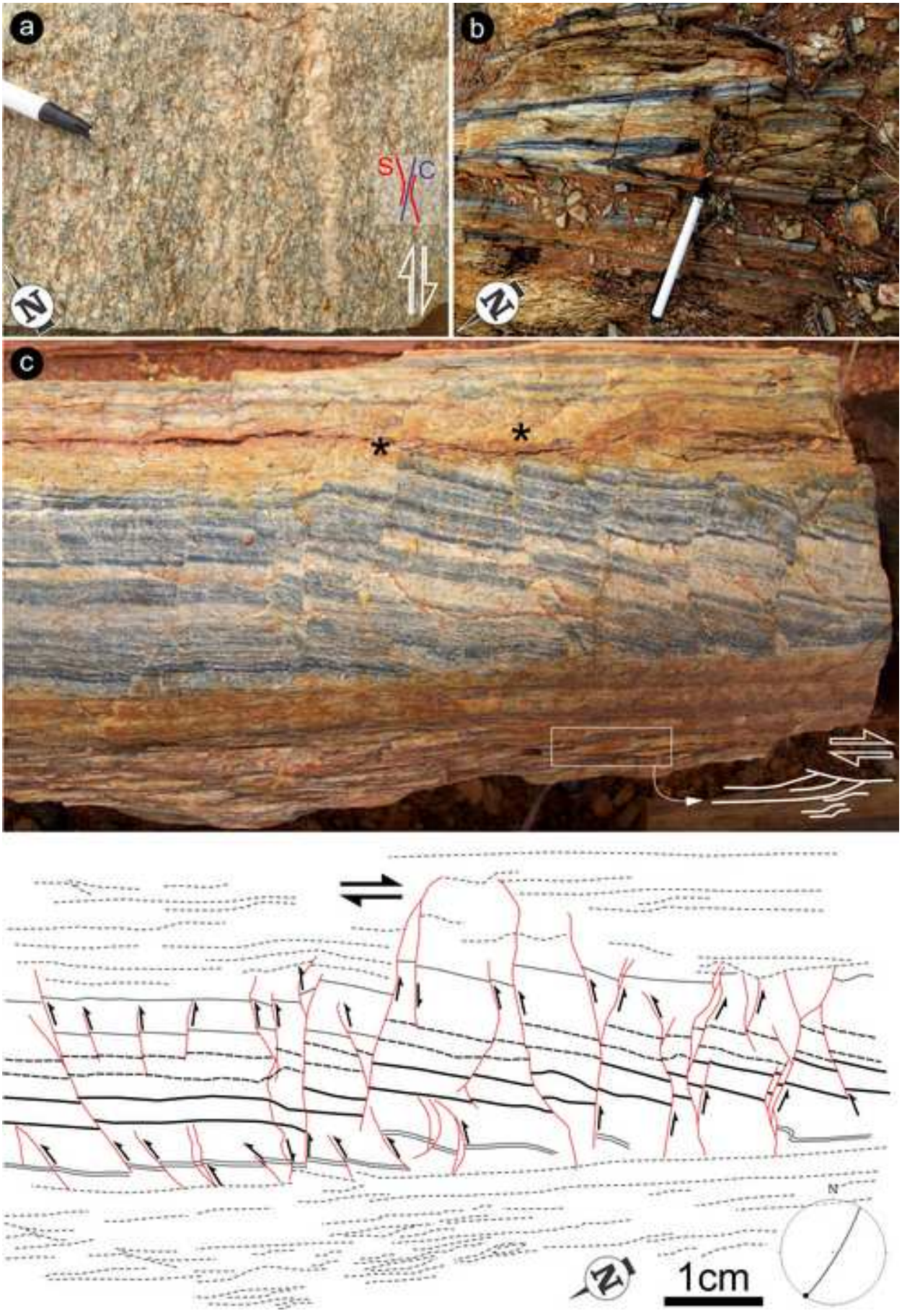

*Figure 9df
Click here to download high resolution image

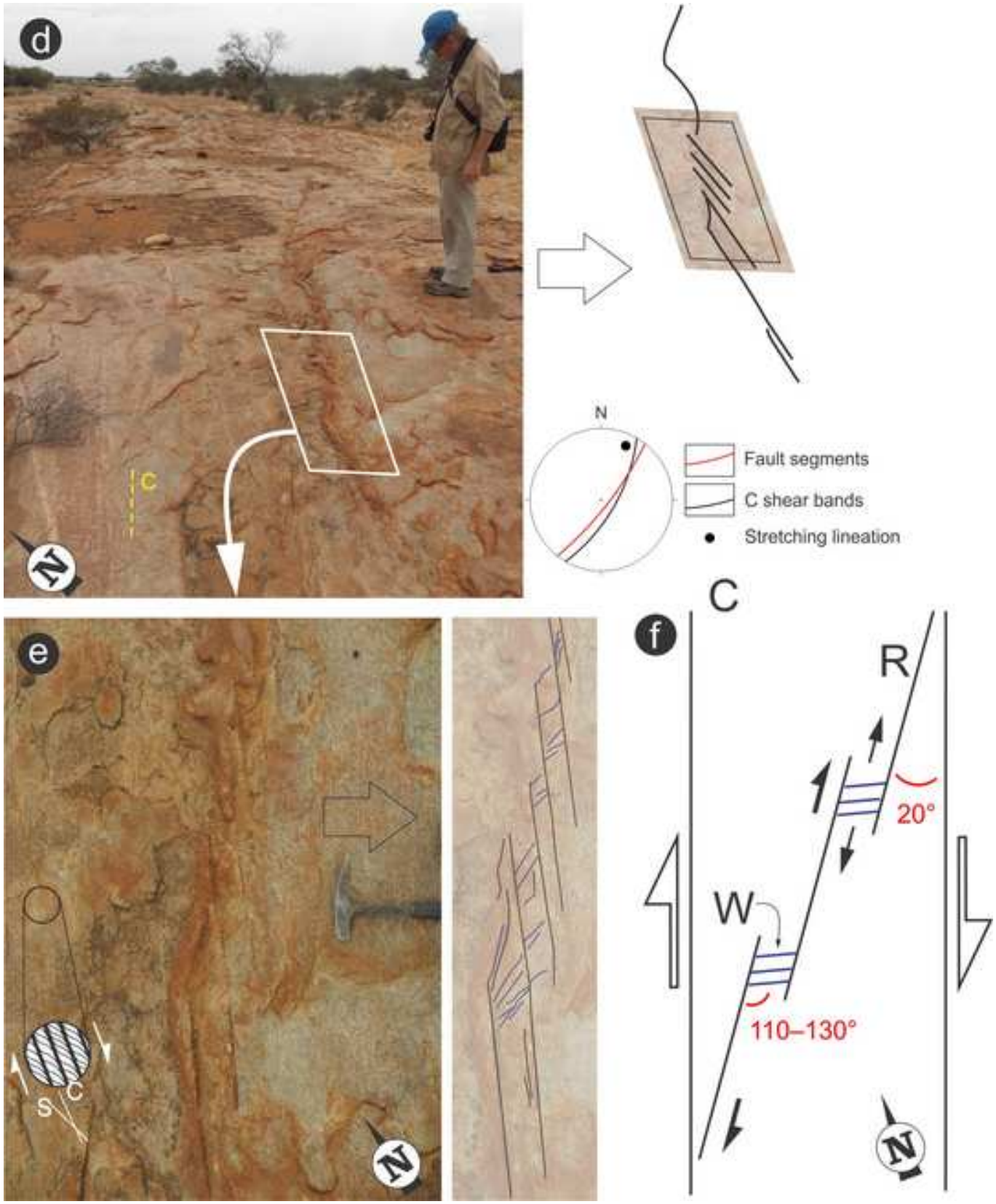

*Figure 10
Click here to download high resolution image

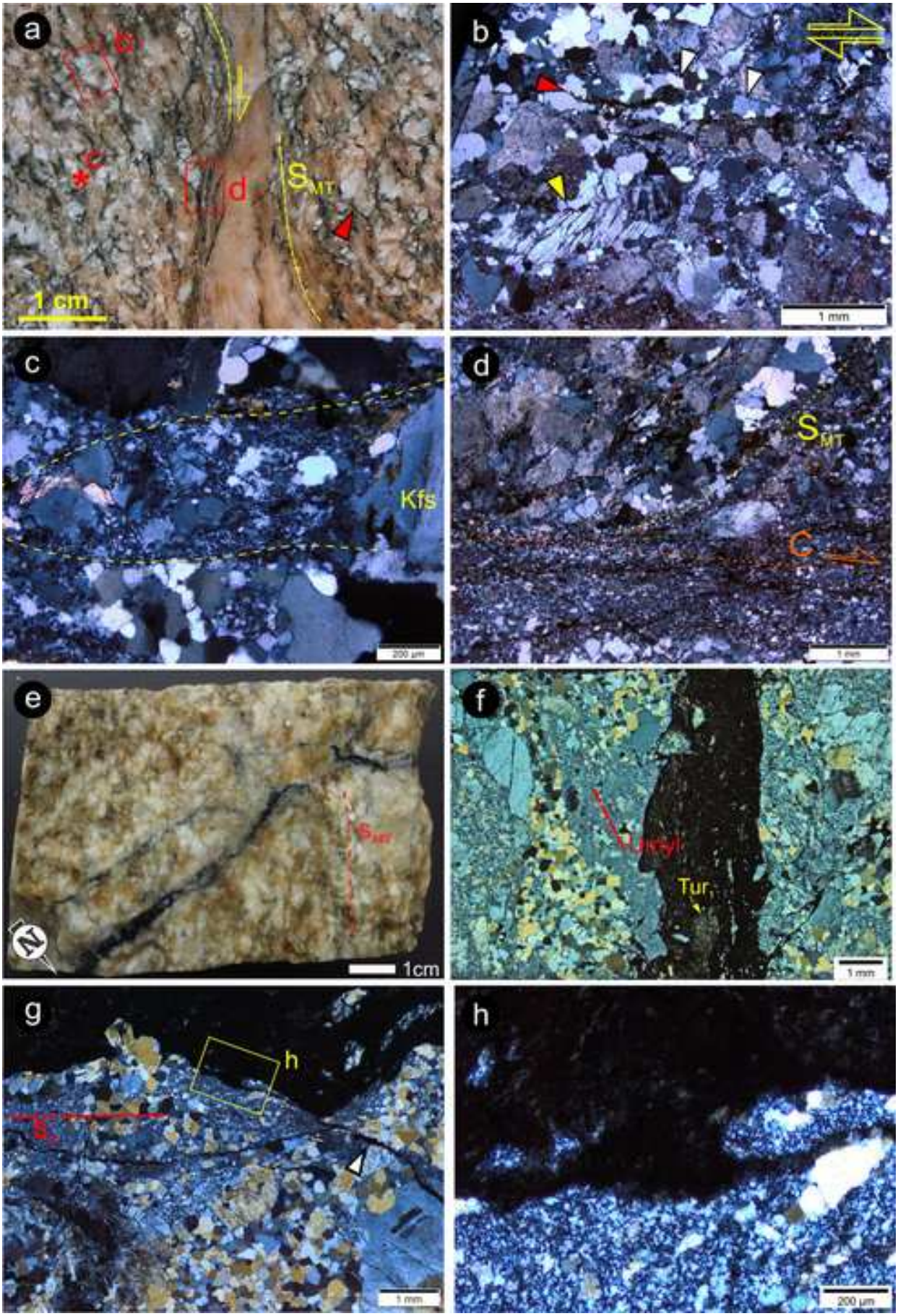

*Figure 11ae
Click here to download high resolution image

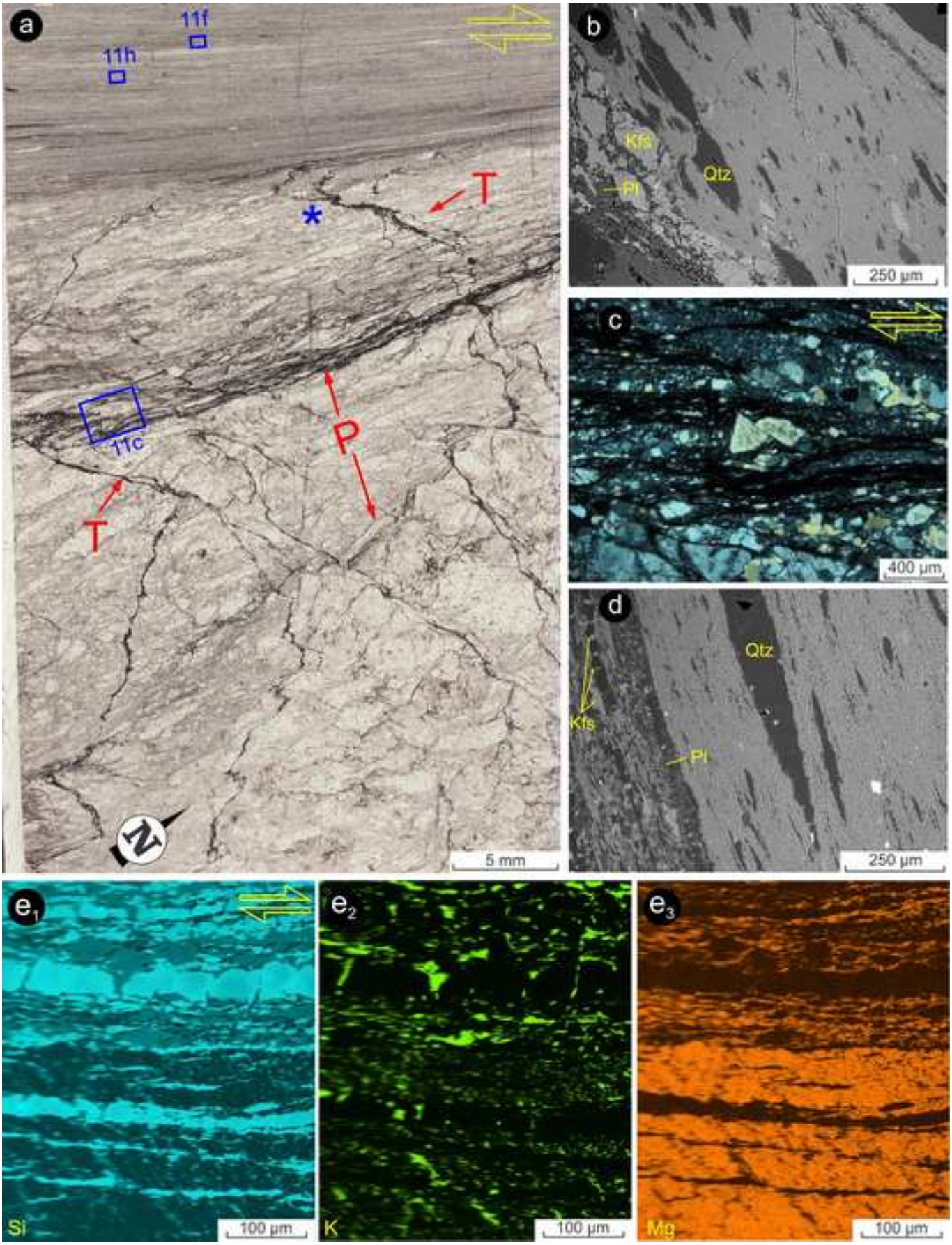

*Figure 11fi
Click here to download high resolution image

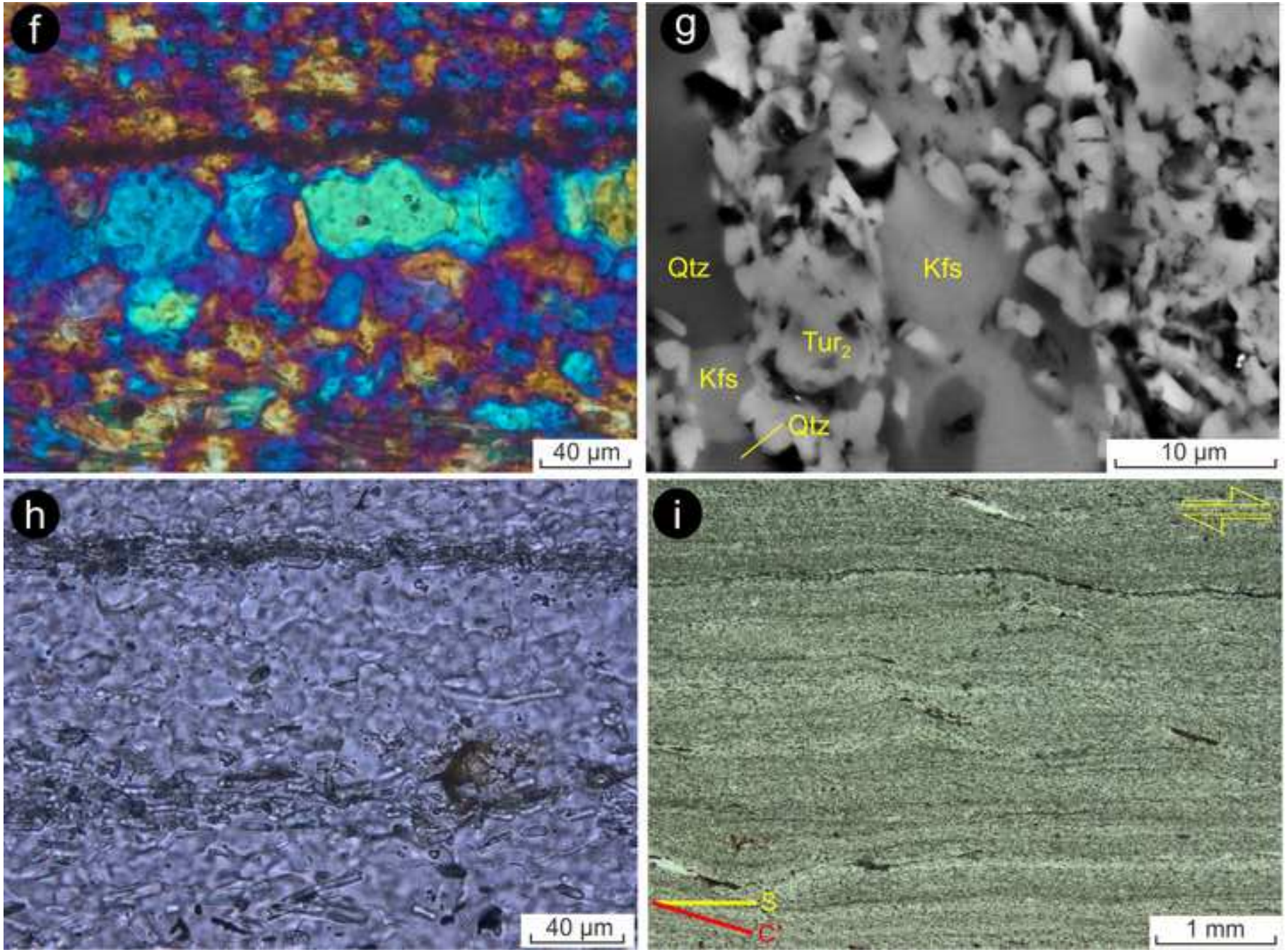

*Figure 12
Click here to download high resolution image

*Figure 13
Click here to download high resolution image